7-20-2018

Phase equilibrium modelling and implications for P-T determinations of medium-temperature UHP eclogites, North Qaidam terrane, China

David Hernández-Uribe
Colorado School of Mines, dav.hernandez.uribe@gmail.com

Chris G. Mattinson
Central Washington University, mattinson@geology.cwu.edu

Jianxin Zhang
Chinese Academy of Geological Sciences Institute of Geology

Recommended Citation

Hernández-Uribe, D, Mattinson, CG, Zhang, J. Phase equilibrium modelling and implications for P–T determinations of medium-temperature UHP eclogites, North Qaidam terrane, China. J Metamorph Geol. 2018; 36: 1237– 1261. https://doi.org/10.1111/jmg.12444

Received: 1 February 2018 | Revised: 16 July 2018

DOI: 10.1111/jmg.12444

ORIGINAL ARTICLE

WILEY Journal of METAMORPHIC GEOLOGY

Phase equilibrium modelling and implications for *P–T* determinations of medium-temperature UHP eclogites, North Qaidam terrane, China

David Hernández-Uribe[1] | **Chris G. Mattinson**[2] | **Jianxin Zhang**[3]

[1]Department of Geology and Geological Engineering, Colorado School of Mines, Golden, Colorado

[2]Department of Geological Sciences, Central Washington University, Ellensburg, Washington

[3]Institute of Geology, Chinese Academy of Geological Sciences, Beijing, China

Correspondence
David Hernández-Uribe, Department of Geology and Geological Engineering, Colorado School of Mines, 1500 Illinois St, Golden, CO 80401.
Email: dav.hernandez.uribe@gmail.com

Funding information
National Science Foundation, Grant/Award Number: NSF-EAR1347433; Geological Society of America; National Natural Science Foundation of China, Grant/Award Number: 41630207; GSA Mineralogy Geochemistry Petrology and Volcanology

Handling Editor: Richard White

ABSTRACT

In contrast to low-*T* eclogites (garnet growth zoning preserved) or high-*T* eclogites (garnet diffusionally homogenized at peak conditions), medium-temperature eclogites pose additional challenges to *P–T* determinations due to the partial preservation of garnet zoning. The Dulan area, in the southeastern part of North Qaidam ultrahigh-pressure terrane, exposes minor eclogites hosted by ortho- and paragneisses. Four fresh, medium-temperature eclogites contain the paragenesis Grt+Omp+Rt+Qz/Coe+Ph±Ky±Zo. In all samples, garnet X_{Mg} shows little zoning, suggesting diffusional modification, and precludes the use of pyrope+almandine+grossular isopleth intersections to determine a *P–T* path. However, in one sample, sharp zoning in grossular content suggests that grossular growth compositions are preserved. Since garnet pyrope+almandine compositions appear to be modified, we instead use the intersections of grossular and garnet volume isopleths to define a prograde *P–T* path. This approach yields a path from ~17 kbar and ~410°C to ~35 kbar and ~625°C with a gradient of ~5–9°C/km through the lawsonite stability field. Peak *P–T* conditions determined from the intersection between Si pfu in phengite and Zr-in-rutile isopleths are ~26–33 kbar and ~625–700 °C for the four eclogites. These conditions are close to the limit of the lawsonite stability field, suggesting that fluid released from lawsonite breakdown may have promoted re-equilibration at these conditions. These peak conditions are also in good agreement (within 3 kbar and 50°C) with garnet–omphacite–phengite (±kyanite) thermobarometry in three of the four samples. We regard the phengite–rutile constraints as more reliable, because they are less sensitive to uncertainties associated with ferric iron compared to conventional thermobarometry. Phase equilibrium modelling predicts that the retrograde assemblage of amphibole+zoisite formed at ~60 km. Infiltration of external fluids was likely required for the growth of these hydrous minerals. Based on the comparison of *P–T* estimation methods applied in this study, we propose that the garnet grossular+volume isopleths can recover the prograde *P–T* path of medium-temperature eclogites, and that the combination of phengite+rutile isopleths represents a more robust approach to constrain peak *P–T* conditions.

KEYWORDS
Dulan area, North Qaidam UHP terrane, phase equilibrium modelling, UHP eclogites, Zr-in-rutile thermometry

1 | INTRODUCTION

Ultrahigh-pressure (UHP) eclogites are products of subduction to mantle depths (Chopin, 2003; Gilotti, 2013). Mineral assemblages preserved in these rocks record metamorphism taking place in the subducting slab which can be used to place constraints on the *P–T* evolution of UHP terranes, leading to the better understanding of large-scale geodynamic processes (e.g., Hacker, Abers, & Peacock, 2003; Poli & Schmidt, 2002). However, medium-temperature eclogites (MT; 650–750°C) pose additional challenges to *P–T* determinations due to the partial preservation of garnet zoning, in contrast to low-*T* eclogites (garnet growth zoning preserved) or high-*T* eclogites (garnet diffusionally homogenized at peak conditions).

Phase equilibrium diagrams have proven to be a powerful approach to obtain robust *P–T* information and elucidate phase relations in metabasic rocks (e.g., Rebay, Powell, & Diener, 2010; Wei & Clarke, 2011). However, the relatively simple mineral assemblages typical of eclogites (i.e., garnet+omphacite) represent a challenge for phase equilibrium modelling and conventional thermobarometry because the compositions and proportions of minerals changes slowly within the garnet+omphacite field (>17 kbar; e.g., Groppo, Rolfo, Liu, Deng, & Wang, 2015; Hacker, 2006; Krogh Ravna & Terry, 2004; Štípská & Powell, 2005). Trace element thermometry is independent of the data, assumptions, and uncertainties of phase equilibrium modelling and conventional thermobarometry, and therefore can improve the precision of the peak temperature constraints. In contrast to peak *P–T* evidence, the prograde *P–T* record is more susceptible to diffusional modification of the mineral compositions by elevated temperatures at peak stages, but slow diffusing elements should better preserve prograde evidence (Caddick, Konopásek, & Thompson, 2010; Konrad-Schmolke, Handy, Babist, & O'Brien, 2005).

The North Qaidam UHP terrane, in China, represents an early Palaeozoic continental suture zone (Figure 1a; Zhang, Yu, & Mattinson, 2017). The Dulan area, in the southeastern part of the North Qaidam terrane (Figure 1a,b), experienced a *c.* 20 Ma UHP event and *c.* 38 Ma of HP metamorphism at *P–T* conditions of ~27–35 kbar and ~610–830°C (Mattinson, Menold, Zhang, & Bird, 2007; Mattinson, Wooden, Liou, Bird, & Wu, 2006; Song, Niu, Su, Zhang, & Zhang, 2014; Song et al., 2003). Despite many studies of peak *P–T* conditions, few studies have addressed the prograde *P–T* path. Existing *P–T* paths from eclogites of the Dulan UHP area have been used to suggest two contrasting hypotheses: (a) One hypothesis suggests that the Dulan area experienced an isothermal prograde path from the amphibolite facies to eclogite facies (Ren et al., 2016; Zhang, Ellis, Christy, Zhang, & Song, 2010), whereas (b) Mattinson et al. (2006) reported pseudomorphs after lawsonite in garnet, interpreted as a cold subduction prograde path.

In this paper, we evaluate and discuss the applicability of phase equilibrium modelling, conventional thermobarometry, and Zr-in-rutile thermometry to MT–UHP eclogites. We present a detailed petrological study of four eclogites from the Dulan UHP area in the North Qaidam terrane, explore the prograde and peak *P–T* evolution of the eclogites, and discuss the tectono-metamorphic evolution of the area.

2 | GEOLOGICAL SETTING

The North Qaidam UHP terrane is a ~350 km NW–SE-trending terrane, represents an early Palaeozoic continental suture, and preserves UHP evidence in eclogites, peridotites, and quartzofeldspathic gneisses at multiple locations (Song et al., 2003, 2014; Zhang et al., 2017). This terrane is bounded on the northeast by the Qilian terrane, and on the southwest by the Qaidam basin (Figure 1a; Mattinson et al., 2007). The North Qaidam eclogites are hosted in the Proterozoic Dakendaban Group gneiss (Mattinson et al., 2007; Song et al., 2003). This unit comprises a sequence of metasedimentary and metaigneous rocks locally intruded by granite and granodiorite (Mattinson et al., 2007).

2.1 | Geology of the Dulan area

The Dulan area is located in the southeastern part of the North Qaidam UHP terrane (Figure 1a,b). This area is dominated by paragneisses, pelitic schists, and orthogneisses, with minor eclogites and ultramafic rocks (Mattinson et al., 2007; Song et al., 2003). All these sequences are cut by *c.* 400 Ma granitoids (Figure 1b; Mattinson et al., 2007; Wu et al., 2004). Coesite has been identified as inclusions in zircon from paragneisses (Song et al., 2003, 2006; Yang et al., 2005), and as inclusions in zircon, garnet, and omphacite in eclogites (Figure 1b; Zhang, Mattinson, Yu, Li, & Meng, 2010; Zhang, Meng, Li, & Mattinson, 2009; Zhang, Zhang, Song, & Niu, 2009).

Eclogites from the Dulan area occur as foliated and unfoliated lenses, blocks, and layers within foliated paragneisses (Mattinson et al., 2007; Song et al., 2003, 2014).

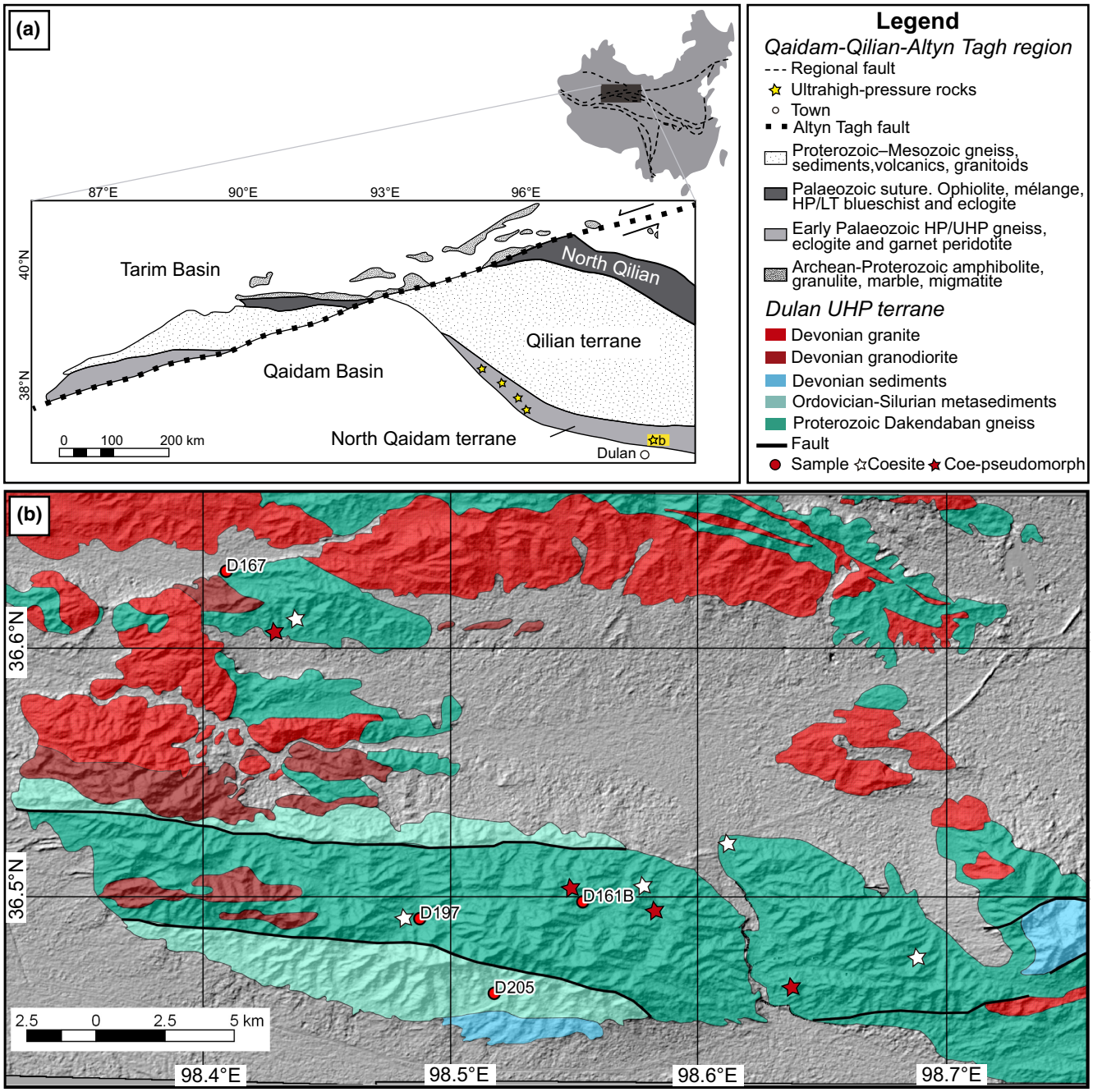

FIGURE 1 Geology of the studied area. (a) Map of China showing the Qaidam–Qilian–Altyn region with the location of UHP rocks in the North Qaidam terrane. The yellow box in the lower right corner of the North Qaidam terrane indicates the location of (b). (b) Simplified geological map of the Dulan area showing the location of eclogite samples analysed in this study. Sample D205 is a float block. Modified from Bureau of Geology and Mineral Resources of Qinghai Province (1968) and Mattinson et al. (2007)

Conventional garnet+omphacite+phengite±kyanite thermobarometry of eclogites records peak *P–T* conditions of ~27–35 kbar and ~610–830°C (Ren et al., 2016; Song et al., 2003, 2006, 2014; Zhang, Mattinson, et al., 2010; Zhang, Meng, et al., 2009; Zhang, Zhang, 2009), and zircon U–Pb ages are *c.* 457–422 Ma (Mattinson et al., 2006; Song et al., 2006, 2014; Zhang, Ellis, Christy, Zhang, & Song, 2010; Zhang, Mattinson, et al., 2010; Zhang, Meng, et al., 2009). Coesite inclusions in zircon from eclogites and paragneiss reveal that the Dulan area experienced a UHP metamorphic event of *c.* 23 Ma, from *c.* 446–423 Ma (Zhang, Mattinson, et al., 2010). Eclogite and host gneiss ages of *c.* 457–422 Ma have been interpreted to indicate a protracted residence at HP–UHP depths (Mattinson, Wooden, Zhang, & Bird, 2009; Mattinson et al., 2006; Zhang, Mattinson, et al., 2010; Zhang et al., 2017). Other authors have interpreted this age range as two different eclogite facies events involving oceanic and continental crust respectively (Ren et al., 2016; Song et al., 2006,

2014; Zhang, Zhang, et al., 2009). Eclogite retrogression is characterized by amphibolite facies overprinting at *P–T* conditions of ~7–9 kbar and ~645–720°C (Song et al., 2003; Zhang, Zhang, et al., 2009). *HP* granulites, in the western part of the Dulan area, record *P–T* conditions of ~15–20 kbar and ~800–950°C, and have been interpreted to represent the thickened part of the overriding plate, or overprinted eclogites from the south part of the Dulan area (Song et al., 2003, 2006; Yu, Zhang, & García del Real, 2011; Yu et al., 2014; Zhang et al., 2017). Ages from HP granulites are *c.* 435–410 Ma, and overlap with the ages of eclogite facies metamorphism (Yu et al., 2014; Zhang et al., 2015).

3 | PETROGRAPHY AND MINERAL CHEMISTRY

3.1 | Analytical methods

To constrain the metamorphic evolution of the Dulan area, four eclogites were selected that contain well-preserved peak mineral assemblages, textures, and assemblages suitable for thermodynamic modelling (i.e., including kyanite and/or phengite; Figure 1b). Mineral proportions were obtained by image analysis of BSE mosaics of whole thin sections using JMicroVision software (Roduit, 2008), and were refined with visual estimations where the BSE brightness is similar for different minerals (e.g., kyanite, quartz). X-ray maps and major element mineral chemistry analyses were performed using a five-spectrometer JEOL JXA-8500F field emission electron microprobe housed at Washington State University. Well-characterized natural and synthetic materials were used as standards for calibration, and a ZAF correction routine was applied. The operating conditions were: accelerating voltage of 15 keV, beam current of 20 nA, and beam diameter of 10 μm for mica and 3 μm for the rest of the minerals.

Epidote-group minerals are identified as zoisite where $X_{Fe}^{3+}=Fe^{3+}/(Fe^{3+}+Al)\leq 0.05$, and as epidote where $X_{Fe}^{3+}>0.05$ (Franz & Liebscher, 2004). Mineral abbreviations used in the text, figures, and tables follow the nomenclature proposed by Whitney and Evans (2010).

3.2 | Results

Dulan eclogites commonly present a well-developed eclogitic foliation formed by oriented garnet, omphacite,

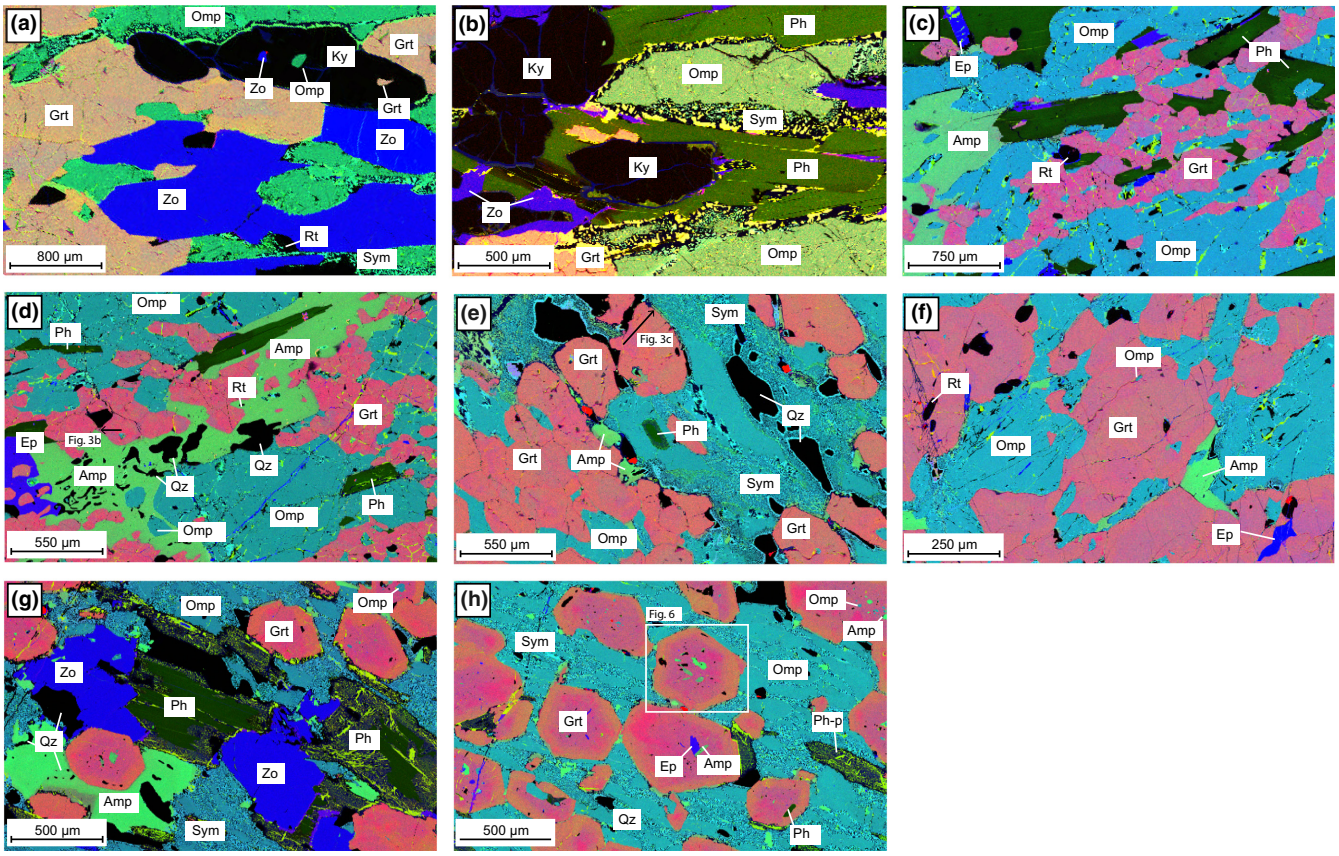

FIGURE 2 Representative mineral assemblages and textural features from: (a, b) eclogite D197, (c, d) eclogite D205, (e, f) eclogite D167, and (g, h) eclogite D161B. All figures are X-ray composite maps (Red = Fe-rich compositions, Green = Mg-rich compositions, Blue = Ca-rich compositions). Colour intensities are comparable between minerals in the same figure but not with the other figures. Black arrows show the location of the compositional profiles shown in Figure 3. The white box in h shows the location of the garnet in Figure 6. p: pseudomorph

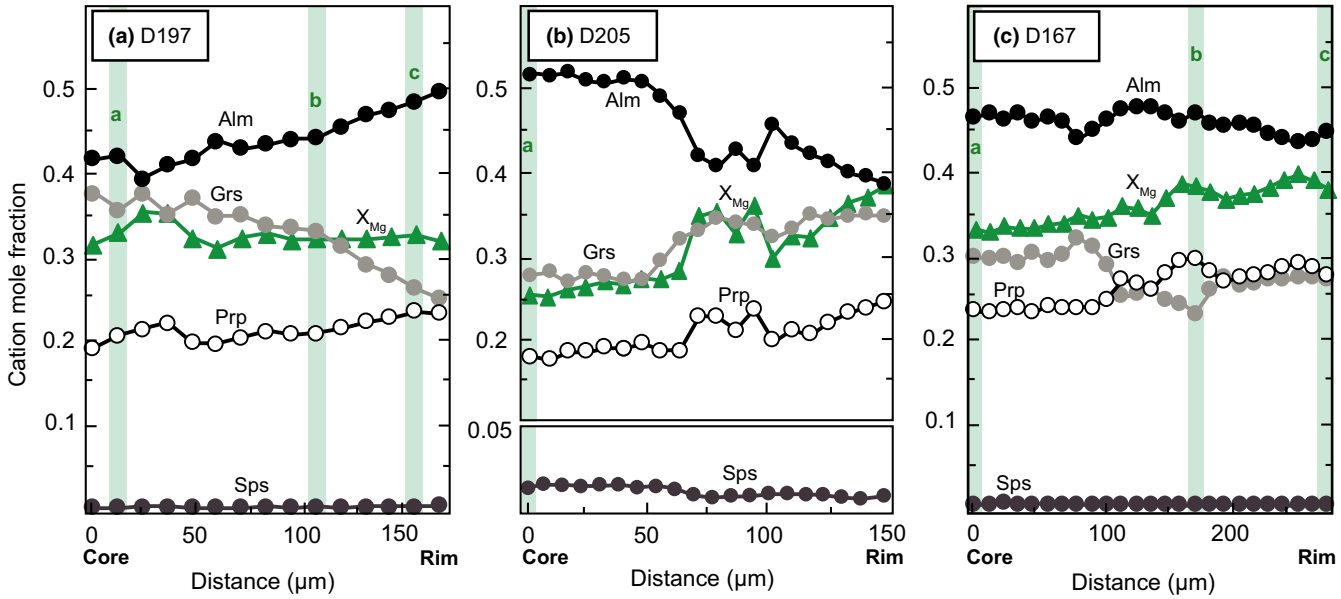

FIGURE 3 Selected garnet core-rim compositional profiles from: (a) eclogite D197, (b) eclogite D205, and (c) eclogite D167. The locations of the profiles are shown with black arrows in Figure S1a and Figure 2d,e respectively. Shaded regions correspond to points shown in Figures S3–S5 respectively

rutile, and in some samples kyanite, zoisite, phengite, and amphibole as well (Figure 2). Fractures filled with secondary quartz, calcite, and/or epidote cut the foliation, and are associated with alteration of the primary eclogitic mineral assemblage to fine grained symplectites (Figure 2).

3.2.1 | Phengite–zoisite–kyanite eclogite D197

Sample D197 was collected in the central part of the southern Dulan area (N36.4915°, E98.4877°; Figure 1b). This coarse-grained eclogite is composed of garnet (~30%), omphacite (~35%), rutile (~2%), kyanite (~15%), phengite (~5%), and zoisite (~13%), with minor amounts of quartz, apatite, and calcite.

Garnet occurs as xenomorphic elongated inclusion-poor crystals up to ~1 mm long (Figure 2a). Garnet is typically clustered with omphacite, rutile, and other garnet. In some garnet clusters (up 2.5 mm in size), individual grains are indistinguishable in the X-ray maps (Figure 2a). Most garnet is compositionally homogeneous, but a few crystals show moderate zoning, with increasing Prp (~20–24%) and Alm (~40–50%), and decreasing Grs (~38–25%) from core to rim; Sps and X_{Mg} show little zoning (Figure 3a; Table 1).

Hypidiomorphic omphacite varies in size from 800 μm to porphyroblasts of 10 mm (Figure 2a,b). Omphacite is partially replaced by symplectites of Cpx+Pl along the grain boundaries and fractures (Figure 2a,b). Some omphacite contains quartz pseudomorphs after coesite (Figure 4a). Omphacite has X_{Mg} = 0.77–0.88, Jd = 0.47–0.62, and low Acm = 0–0.1 (Figure 5a; Table 1).

Phengite occurs as ~1 mm hypidiomorphic–idiomorphic crystals (Figure 2b). Rare crystals are rimmed by fine-grained

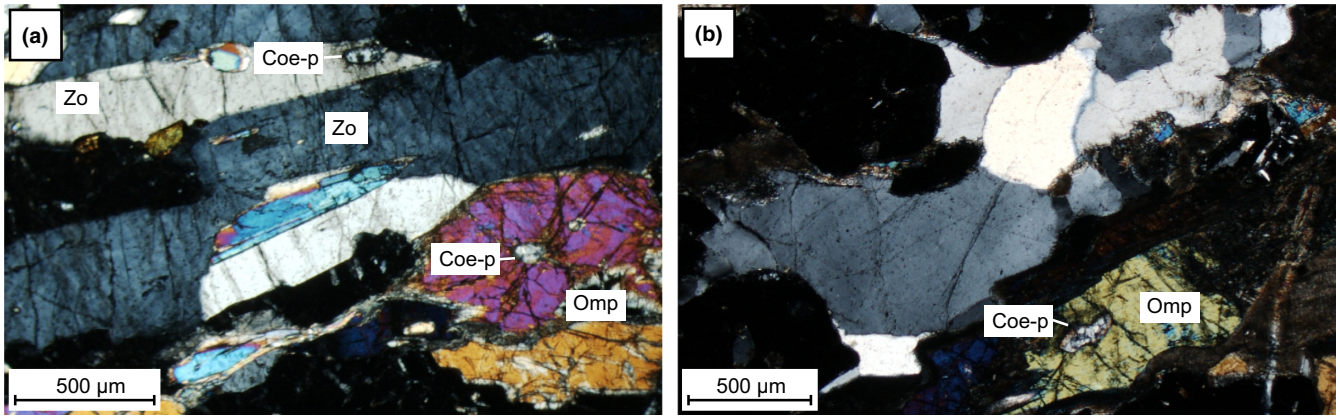

FIGURE 4 Quartz pseudomorphs after coesite in eclogite (a) D197 and (b) D167. p: pseudomorph

TABLE 1 Representative microprobe analyses for studied eclogites from the Dulan area, China

Sample	D197				D205				D167				D161B			
Mineral		Grt	Omp	Ph		Grt	Omp	Ph		Grt	Omp	Ph		Grt	Omp	Ph
Location	core	rim	mx	mx	core	rim	mx	mx	core	rim	mx	i	core	rim	mx	mx
Analysis	1620	1607	1419	1367	1285	1269	1234	1111	1666	1688	1753	1635	740	712	775	826
SiO_2	39.29	38.94	56.24	49.88	38.44	39.20	55.76	52.26	39.01	39.47	55.55	53.15	38.76	39.33	55.16	52.14
TiO_2	0.04	0.04	0.13	0.51	0.03	0.02	0.04	0.36	0.07	0.03	0.07	0.44	0.11	—	0.05	0.42
Al_2O_3	22.14	21.98	14.79	29.53	21.60	21.96	9.95	25.14	21.77	21.92	8.59	26.19	21.72	22.19	8.21	27.63
Cr_2O_3	—	—	—	—	0.01	0.04	0.24	0.05	0.05	0.08	0.06	0.05	0.07	0.05	0.03	0.10
FeO	19.98	23.19	3.18	1.31	24.23	18.96	2.94	1.64	21.93	20.35	3.39	0.72	21.56	21.56	3.42	1.43
MnO	0.30	0.37	—	—	0.69	0.34	0.00	—	0.40	0.36	—	—	0.74	0.37	0.01	0.04
MgO	5.14	6.23	6.44	3.37	4.79	6.27	9.99	4.54	6.03	7.58	10.68	4.58	4.76	8.49	11.16	3.00
CaO	13.85	9.66	10.85	—	9.68	12.85	14.95	—	10.73	9.88	15.93	0.02	12.64	7.84	16.72	0.66
Na_2O	0.04	0.01	7.88	0.74	—	0.02	5.69	0.31	0.03	—	5.02	0.33	0.04	0.02	4.67	1.59
K_2O	—	0.01	—	9.86	—	0.01	—	10.29	—	—	0.01	10.22	—	—	—	9.22
Total	100.77	100.43	99.50	95.21	99.47	99.67	99.57	94.60	100.03	99.66	99.30	95.70	100.41	99.85	99.44	96.22
Oxygen	12	12	6	11	12	12	6	11	12	12	6	11	12	12	6	11
Si	3.00	2.99	1.99	3.32	3.01	3.00	1.99	3.51	3.00	3.02	2.00	3.53	2.99	3.00	1.98	3.43
Ti	—	—	—	0.03	—	—	—	0.02	—	—	—	0.02	0.01	—	—	0.02
Al	1.99	1.99	0.62	2.32	1.99	1.98	0.42	1.99	1.97	1.98	0.36	2.05	1.96	1.99	0.35	2.14
Cr	—	—	—	—	—	—	0.02	—	0.01	0.01	—	0.01	0.01	0.01	—	0.02
Fe^{3+}	0.02	0.03	—	—	—	0.01	—	—	0.02	—	—	—	0.05	0.01	0.01	—
Fe^{2+}	1.25	1.46	0.09	0.07	1.58	1.20	0.09	0.09	1.39	1.30	0.10	0.04	1.34	1.36	0.09	0.08
Mn	0.02	0.02	—	—	0.05	0.02	—	—	0.03	0.02	—	—	0.05	0.02	—	—
Mg	0.58	0.71	0.34	0.33	0.56	0.72	0.53	0.46	0.69	0.86	0.57	0.45	0.55	0.96	0.60	0.29
Ca	1.13	0.79	0.41	—	0.81	1.05	0.57	—	0.88	0.81	0.61	—	1.04	0.64	0.64	0.05
Na	0.01	—	0.54	0.10	—	—	0.39	0.04	0.01	—	0.35	0.04	0.01	—	0.32	0.20
K	—	—	—	0.84	—	—	—	0.88	—	—	—	0.87				0.77
Sum	8.0	8.0	4.0	7.0	8.0	8.0	4.0	7.0	8.0	8.0	4.0	7.0	8.0	8.0	4.0	7.0
X_{Mg}	0.32	0.33	0.79	0.83	0.26	0.38	0.85	0.84	0.33	0.40	0.85	0.92	0.29	0.41	0.88	0.78
Sps	0.01	0.01	—	—	0.02	0.01	—	—	0.01	0.01	—	—	0.02	0.01	—	—
Prp	0.19	0.24	—	—	0.19	0.24	—	—	0.23	0.29	—	—	0.18	0.32	—	—
Grs	0.38	0.27	—	—	0.27	0.35	—	—	0.29	0.27	—	—	0.35	0.21	—	—
Alm	0.42	0.49	—	—	0.53	0.40	—	—	0.46	0.43	—	—	0.45	0.46	—	—
Jd	—	—	0.56	—	—	—	0.40	—	—	—	0.35	—	—	—	0.32	—
X_{Na}	—	—	—	0.11	—	—	—	0.04	—	—	—	0.04	—	—	—	0.21

mx = matrix; i = inclusion; X_{Mg}=Mg/(Mg+Fe^{2+}); Grs=Ca/(Ca+Fe^{2+}+Mn+Mg); Prp=Mg/(Ca+Fe^{2+}+Mn+Mg); Alm=Fe/(Ca+Fe^{2+}+Mn+Mg); Sps=Mn/(Ca+Fe^{2+}+Mn+Mg); X_{Na}=Na/(K+Na); Jd = jadeite content following the classification of Morimoto (1988). Ferric iron calculated by charge balance.

symplectites of Bt+Pl (Figure 2b). Also, phengite is partially replaced by chlorite along cleavages and grain boundaries. Phengite yields Si pfu = 3.18–3.33, X_{Mg} = 0.78–0.96, and X_{Na} = 0.09–0.19 (Figure 5b; Table 1). Rare phengite grains are weakly zoned, with Si-rich cores and Si-poor rims.

Kyanite is present as elliptical xenomorphic crystals up to 500 μm to 1 mm long (Figure 2a,b). This mineral displays twinning, and preserves zoisite, garnet, and omphacite (Jd = 0.56–0.63) inclusions (Figure 2a). Kyanite is rimmed by fine-grained symplectites, formed by Pg (Si = 2.94 pfu and X_{Na} = 0.86–0.98)+Pl.

Zoisite (X_{Fe}^{3+} = 0.01–0.04; Figure S1 and Table S1) occurs as ~800 μm idiomorphic to hypidiomorphic crystals (Figure 2a,b). This mineral shows straight grain boundaries with garnet, omphacite, and kyanite (Figure 2a). Zoisite grains are inclusion-free, colourless, and some are included

in kyanite. In some areas, zoisite appears to be growing along the grain boundaries within the kyanite (Figure 2b). Zoisite presents first order interference colours, and some grains display anomalous blue interference colours. Scarce crystals have oscillatory zoning. Some zoisite grains contain quartz pseudomorphs after coesite (Figure 4a).

3.2.2 | Phengite eclogite D205

Eclogite D205 was collected from a boulder located within a drainage in the metasedimentary unit (N36.4614°, E98.5177°; Figure 1b), but it is inferred to originate from an upstream outcrop of the eclogite-bearing unit in the southern part of the Dulan area. Sample D205 is a coarse-grained eclogite composed of garnet (~20%), omphacite (~35%), phengite (~15%), amphibole (~15%), epidote (~8%), rutile (~3%), and quartz (4%), with minor amounts of apatite. Ilmenite is the most common opaque mineral in the sample.

Garnet occurs as xenomorphic to hypidiomorphic inclusion-free crystals and clumps up to 250–750 μm long (Figure 2c,d). Garnet, as well as omphacite, form polygonal aggregates where the eclogite displays a granoblastic texture (Figure 2c). Garnet shows moderate chemical zoning, characterized from core to rim by increasing X_{Mg} (0.26–0.38), Prp (~19–24%), and Grs (~27–35%) and by decreasing Sps (~1.5–0.7%) and Alm (~53–40%; Figure 3b; Table 1).

Omphacite occurs as hypidiomorphic crystals 500–750 μm long (Figure 2c). Omphacite is partially replaced by fine-grained symplectites of Cpx+Pl (Figure 2c,d). Omphacite has X_{Mg} = 0.84–0.89, Jd = 0.36–0.40, and Acm = 0–0.04 (Figure 5a; Table 1).

Phengite occurs as hypidiomorphic–idiomorphic crystals 0.7–2.5 mm long (Figure 2c,d). Phengite is rimmed by fine-grained symplectites. Phengite yields Si pfu = 3.22–3.55, X_{Na} = 0.02–0.16, and X_{Mg} = 0.75–0.84 (Figure 5b; Table 1). This mineral is strongly zoned, with Si-Mg-rich cores and Si-Mg-poor rims (Figure 5b).

Epidote (X_{Fe}^{3+} = 0.10–0.13; Figure S1 and Table S1) occurs as hypidiomorphic to xenomorphic crystals 0.45–5 mm long (Figure 2c,d). Epidote contains garnet and amphibole inclusions, and epidote grains are included in amphibole poikiloblasts (Figure 2c,d). Epidote is colourless, presents first order interference colours, and some grains display anomalous blue interference colours. The presence of epidote with high interference colours is spatially related to opaque minerals and red oxides.

Amphibole occurs as xenomorphic poikiloblasts up to ~5 mm long (Figure 2d). Inclusions of garnet, omphacite, phengite, epidote, and rutile are common in this mineral (Figure 2c,d). Some amphibole crystals show spongy quartz-amphibole intergrowths, and replace omphacite (Figure 2d). Amphibole is strongly zoned, from Mg-katophorite cores to edenite rims (Figure S1 and Table S1).

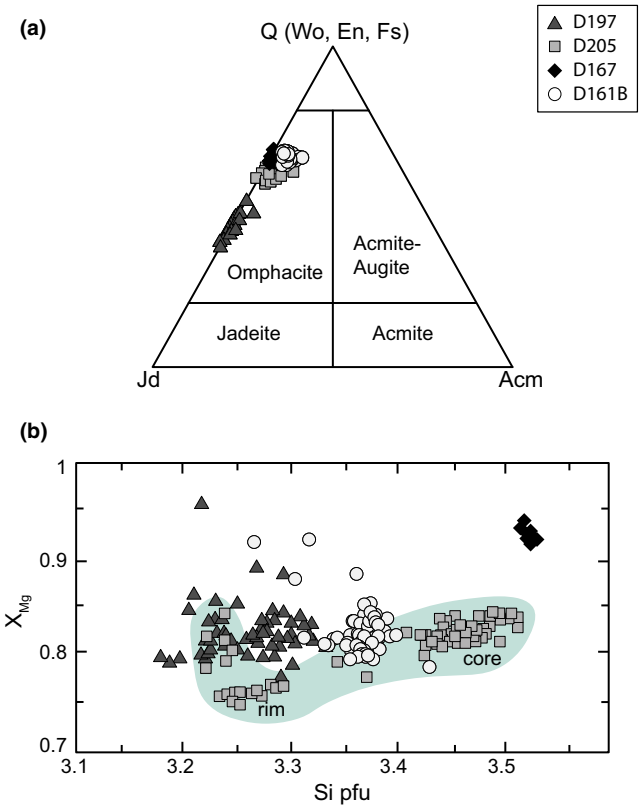

FIGURE 5 (a) Classification diagram for Na and Na-Ca clinopyroxene following Morimoto (1988). (b) Phengite X_{Mg} versus Si pfu. Note the strong X_{Mg} and Si zoning of phengite in eclogite D205 (shown in the shaded area). Both figures share the same symbology. X_{Mg} = Mg/(Mg+Fe^{2+})

3.2.3 | Phengite eclogite D167

Eclogite D167 was collected in the northern part of the Dulan area (N36.6316°, E98.4096°; Figure 1b). This medium coarse-grained eclogite is composed of garnet (~35%), omphacite (~35%), rutile (~3%), phengite (~2%), amphibole (~10%), quartz (~5%), and epidote (~10%), with minor amounts of apatite.

Garnet occurs as xenomorphic elongated crystals 400 μm to 1 mm long (Figure 2e,f). Some grains preserve omphacite inclusions (Figure 2f). Most garnet grains are homogenous in composition, yet rare crystals show moderate zoning with increasing X_{Mg} (~0.33–0.40), Prp (~23–27%), and decreasing Grs (~30–27%) from core to rim; Alm and Sps show little zoning (Figure 3c; Table 1).

Hypidiomorphic omphacite varies in size from 0.5 to 1.5 mm long (Figure 2e,f). Omphacite is partially replaced by symplectites of Cpx+Pl (Figure 2e,f). Rare omphacite contains quartz pseudomorphs after coesite (Figure 4b). Omphacite yields X_{Mg} = 0.85–0.89, Jd = 0.32–0.34, and Acm = 0–0.03 (Figure 5a; Table 1).

Phengite occurs as ~250 μm elongated crystals (Figure 2e). Phengite grains are rare, and are mostly found as

inclusions in omphacite and garnet; matrix crystals are completely replaced by fine-grained symplectites of Bt+Pl (Figure 2e). Phengite yields Si pfu = 3.52–3.53, X_{Mg} = 0.92–0.94, and X_{Na} = 0.04–0.05 (Figure 5b; Table 1).

Epidote (X_{Fe}^{3+} = 0.06–0.15; Figure S1 and Table S1) occurs as oriented hypidiomorphic to xenomorphic crystals up to ~250 μm long (Figure 2f). Epidote appears in the matrix; in some areas, it is unclear if epidote is sited on grain boundaries within garnet clusters or if it forms inclusions in garnet (Figure 2f). Most epidote is inclusion-free, presents first-order interference colours, and some grains display anomalous blue interference colours. Scarce grains contain omphacite and garnet inclusions. Some crystals display strong compositional zoning with low-Ca and high-X_{Fe}^{3+} cores, and high-Ca and low-X_{Fe}^{3+} rims (Figure S1 and Table S1). Low-Ca content in the crystallographic A-site suggests the presence of REE and/or Sr.

Amphibole occurs as intergranular crystals 500–750 μm long, typically replacing omphacite (Figure 2e,f). Amphibole in this eclogite is hornblende and pargasite (Figure S1 and Table S1).

3.2.4 | Phengite eclogite D161B

Eclogite D161B was collected in the central part of the Dulan area (N36.4983°, E98.5534°; Figure 1b). This fine-grained eclogite is composed of garnet (~30%), omphacite (~35%), rutile (~2%), phengite (~3%), amphibole (~10%), quartz (~5%), and zoisite (~15%) with minor apatite.

Garnet occurs as idiomorphic porphyroblasts 300 μm to 1.5 mm long (Figure 2g,h). Most grains contain phengite, amphibole, and epidote inclusions (Figure 2g,h). Inclusions are constrained to the garnet core and mantle (Figure 2g,h). Garnet presents strong chemical zoning, with an overall increase of X_{Mg} (~0.29–0.41%), Prp (~18–32%), and Alm (~44–48%), and decrease of Grs (~34–23%) and Sps (~2–0.8%) from core to rim (Figure 6; Table 1). Within the mantle, garnet shows a zoning reversal characterized by an increase of grossular and a decrease of pyrope (Figure 6 and Figure S2). Compositional cross-cutting relations (i.e., zoning sharply truncated by resorption surfaces followed by garnet overgrowth of different composition) suggest two phases of garnet growth each bounded by a resorption event (Figure S2). Garnet can be separated into two groups. Garnet 1 includes the grossular-rich core and the zoning reversal in the mantle; these zones are truncated by resorption surface 1. Garnet 2 forms grossular-poor rims; resorption surface 2 locally truncates both garnet 1 and garnet 2 (Figure S2). Omphacite grains are in contact with both resorption surfaces suggesting that the resorption events happened during eclogite facies conditions (Figure S2).

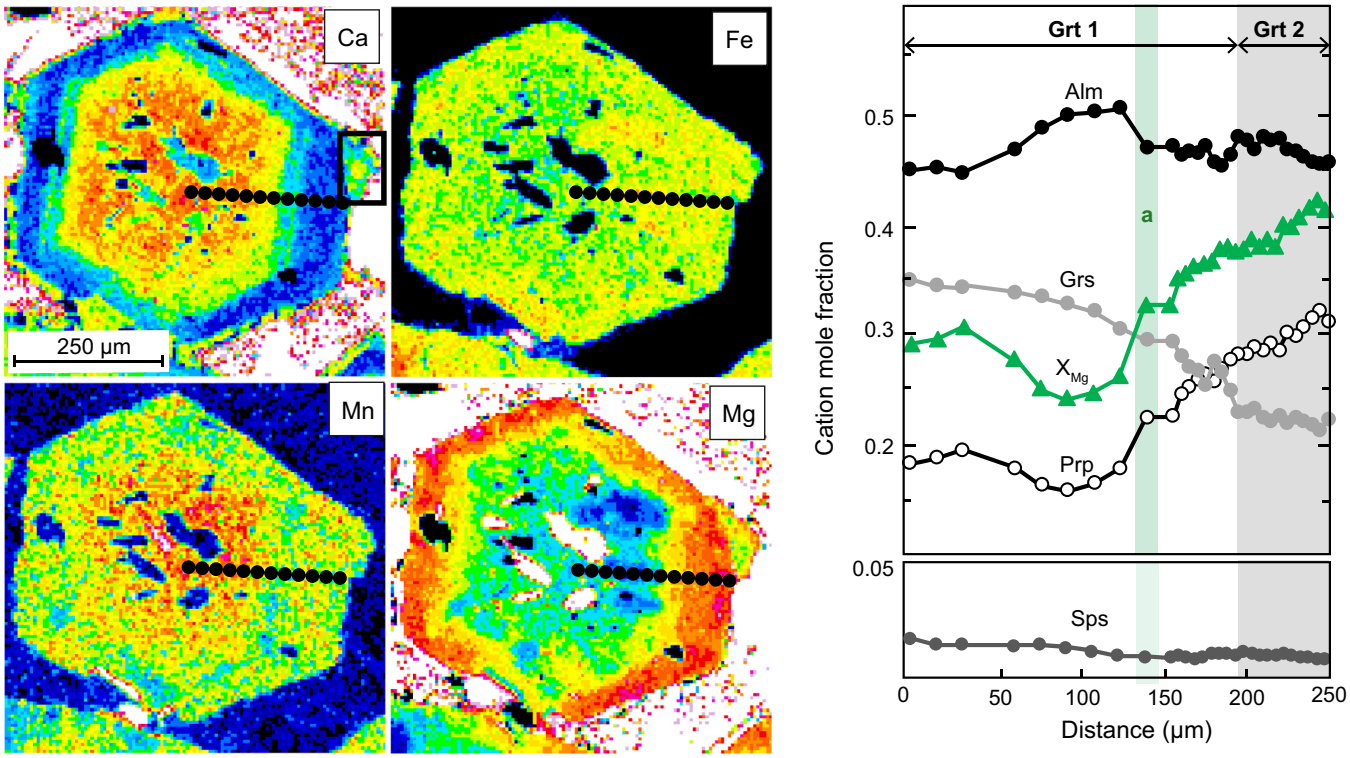

FIGURE 6 Selected garnet X-ray compositional maps and corresponding core-rim profile from eclogite D161B. Warm and cold colours correspond to high and lower concentrations respectively. Colour scale is not the same between the different maps. Black box shows garnet overgrowth with different composition (see text). The location of the X-ray map is shown in a white box in Figure 2h. The green shaded region "a" on the profile corresponds to the "a" point shown in Figure S6. The black arrows on the profile delimit the two different garnet phases (see text and Figure S2)

Omphacite occurs as hypidiomorphic crystals 500–700 μm long (Figure 2g,h). This mineral is partially replaced by symplectites of Cpx+Pl along grain boundaries (Figure 2g,h). Omphacite yields X_{Mg} = 0.84–0.91, Jd = 0.28–0.36, and Acm = 0.01–0.03 (Figure 5a; Table 1).

Phengite occurs as crystals up to 500–800 μm (Figure 2g,h). Phengite grains are rimmed by fine-grained symplectitic intergrowths of Bt+Pl (Figure 2g,h). Phengite reveals Si pfu = 3.27–3.43, X_{Mg} = 0.79–0.92, and X_{Na} = 0.02–0.21 (Figure 5b; Table 1).

Zoisite (X_{Fe}^{3+} = 0.03–0.05; Figure S1 and Table S1) occurs as hypidiomorphic to xenomorphic poikiloblasts up to ~1mm long (Figure 2g). Zoisite porphyroblasts have inclusions of garnet, omphacite, amphibole, rutile, and quartz. Also, epidote (X_{Fe}^{3+} = 0.11–0.13; Figure S1 and Table S1) is present as inclusions in garnet, commonly as multiphase inclusions with amphibole (Figure 2h). Epidote-group minerals present first-order interference colours, and sparse crystals display anomalous blue interference colours.

Amphibole occurs as small grains and porphyroblasts 500–700 μm long. Two inclusions in garnet are barroisite and pargasite, and amphibole in the matrix is hornblende, typically replacing omphacite (Figure S1 and Table S1).

4 | ECLOGITE THERMOBAROMETRY

4.1 | Methods

In order to understand the metamorphic evolution of eclogites from the Dulan area, phase equilibrium modelling was coupled with Zr-in-rutile thermometry and conventional thermobarometry. For samples D197, D205, and D167, fracturing, resorption and recrystallization, and diffusion likely affected garnet (see discussion) obscuring the prograde *P–T* path, but peak conditions and constraints on the retrograde conditions were obtained. For sample D161B, a prograde *P–T* path was obtained using the methodology described below. For all samples, peak conditions were determined using the intersection of the maximum Si pfu in phengite isopleths and Zr-in-rutile isopleths. The *P–T* area showing the observed amphibole and epidote volume is interpreted to be the conditions where the rock stopped recording *P–T* information.

4.1.1 | Calculation parameters for phase equilibrium diagrams

Phase equilibrium diagrams were constructed using Perple_X 6.7.4 (version October 2015; Connolly, 1990, 2009) and the internally consistent thermodynamic data set tcdS55 (Holland & Powell, 1998; updated August 2004). Modelling was performed in the 10-component MnO–Na_2O–CaO–K_2O–FeO–MgO–Al_2O_3–SiO_2–H_2O–O_2 (MnNCKFMASHO) system, using the following activity–composition (*a–x*) relations for solid solution phases: garnet, epidote, and talc (Holland & Powell, 1998); biotite (Powell & Holland, 1999); chlorite (Holland, Baker, & Powell, 1998); white mica (Coggon & Holland, 2002); amphibole (Dale, Powell, White, & Elmer, 2005); and omphacite (Diener & Powell, 2012). Additional pure phases included were lawsonite, kyanite, quartz/coesite, zoisite, and albite. Water was considered to be in excess due to the abundance of hydrous prograde, peak, and retrograde minerals. We acknowledge that the upper temperature limit used in the models may exceed the wet solidus for metabasic rocks, as demonstrated in recently parameterized *a–x* relations for solid solution phases (Green et al., 2016). However, the Green et al. (2016) melt model was calibrated for use at crustal *P–T* conditions (<13 kbar), thus, is unsuitable for examining phase equilibria in the eclogite facies. Furthermore, there is no evidence of partial melting in the studied samples. Uncertainties in the location of the mineral assemblage boundaries of the most *P–T* sensitive assemblages are ±1 kbar and ±50°C (Palin, Weller, Waters, & Dyck, 2016; Powell & Holland, 2008).

The bulk compositions used to perform the phase equilibrium modelling were obtained from XRF, and from modal abundances estimates combined with microprobe analyses (i.e., reconstructed bulk-rock compositions; Table 2). Whole-rock XRF major element data were obtained with a ThermoARL XRF spectrometer housed at Washington State University. The XRF whole-rock compositions were modified to account for the following scenarios: (a) Minerals that were not included in the modelling but their compositions have an important contribution to the whole-rock composition (i.e., apatite). The phosphorus content was decreased to 0%, and CaO was decreased a corresponding amount assuming that phosphorus is bound exclusively in apatite. (b) The effect of ferric iron (Fe^{3+}) on the stability of the mineral assemblages (also modified in reconstructed bulk-rock compositions). Mineral compositions, and *T–X* and *P–X* diagrams (X_{Fe}^{3+} = 0–0.5) were used as a guide to constrain the oxidation state of the samples (Diener & Powell, 2010). A value of X_{Fe}^{3+} = 0.05 was used to construct all diagrams based on satisfactory reproduction of the observed mineral assemblages and compositions of the samples (Table 1).

The prograde path was constructed for sample D161B by modelling the garnet growth, using the intersection between modelled garnet volume isopleths and its corresponding grossular content. Because of the low Ca diffusion rate, its concentration is more likely to represent the original concentration in garnet than Fe, Mg, or Mn (Carlson, 2006; Carlson, Pattison, & Caddick, 2015; Chakraborty & Ganguly, 1992; Chernoff & Carlson, 1997;

TABLE 2 Bulk-rock compositions used for the phase equilibrium modelling (wt%)

Sample	SiO_2	Al_2O_3	FeO	MnO	MgO	CaO	Na_2O	K_2O	H_2O	X_{Fe3+}	Note
D197	46.86	24.77	9.28	0.15	4.87	10.56	3.07	0.39	Excess	0.05	Reconstructed
D205	48.99	16.36	11.15	0.19	8.00	11.67	2.57	1.01	Excess	0.05	m-XRF
D167	48.98	16.10	11.53	0.17	8.43	12.49	2.12	0.18	Excess	0.05	Reconstructed
D161B	50.90	15.40	9.80	0.21	7.90	12.40	2.54	0.80	Excess	0.05	Reconstructed

$X_{Fe3+}=Fe^{3+}/(Fe^{2+}+Fe^{3+})$. reconstructed = reconstructed bulk-rock composition; m-XRF = modified XRF whole-rock data.

Florence & Spear, 1991; Giuntoli, Lanari, & Engi, 2018). To construct the *P–T* path, a garnet was selected with a representative concentric compositional zoning from sample D161B, using different X-ray maps and different garnet core-rim compositional profiles (Figure S2). The selected garnet is shown in Figures 2h and 6, and Figure S2. Each measured grossular composition was assigned to its corresponding cumulative volume value within the garnet. For example, from the core to rim profile, the first analysis has a volume 1 (V_1), calculated using radius 1 (R_1), and a Grs content 1 (X_1). The next point will have a V_2, calculated using R_2, and a corresponding X_2. Finally, the total volume value of the garnet (i.e., 100%) was scaled to the total abundance of garnet in the sample. To calculate the volume, the garnet was assumed to have a dodecahedral shape for the volume calculations. All the information for the 29 points used to build the prograde *P–T* path is shown in Table S2. Garnet fractionation was not accounted for in building the *P–T* path. A test of the effect of garnet fractionation shifted point 29 by ~50°C and ~3 kbar, to lower pressure and temperature. Furthermore, recent studies suggest that chemical fractionation of zoned minerals in metabasic rocks does not have a significant effect on the *P–T* results (St-Onge, Rayner, Palin, Searle, & Waters, 2013). Notwithstanding, we acknowledge that the lack of chemical fractionation will provide a qualitative location of the grossular and volume isopleths.

4.1.2 | Conventional thermobarometry

Conventional thermobarometry was applied to the studied eclogites following Krogh Ravna (2000) and Krogh Ravna and Terry (2004). In order to better constrain the peak conditions, eight possible mineral compositions combinations were used for samples D197, D205, and D161B, and four combinations for eclogite D167. For eclogites D205, D167, and D161B, the garnet–omphacite thermometer and garnet–omphacite–phengite barometer were used. For eclogite D197, the garnet–omphacite–kyanite–phengite-coesite/quartz equilibrium was used. The minerals used for the *P–T* calculations are interpreted to be in textural equilibrium; chosen compositions are from (a) garnet rims (or near rim if the outermost analyses show evidence of back diffusion); (b) omphacite with the highest jadeite content; and (c) phengite with the highest Si pfu. The chemistry of the minerals used for the calculations are shown in Table S3.

4.1.3 | Zr-in-rutile thermometry

Thin sections were examined under reflected-light microscopy and BSE before analytical measurements were made. Rutile was selected avoiding cracks, grain boundaries, bad polishing, and nearby zircon (<100 μm away). Measurements that contain more than 0.3 wt% SiO_2 (suggesting contamination from nearby silicates), overlapped pits, scratches, and/or holes were excluded from the results.

Measurements of rutile compositions were performed using a JEOL JXA-8500F field emission electron microprobe at the GeoAnalytical Lab in Washington State University, utilizing five wavelength-dispersive X-ray spectrometers and ProbeForEPMA data acquisition and reduction software (Probe Software, Inc., Eugene, OR). Accelerating voltage was 15 kV, with a beam diameter of 5 μm, and a beam current of 200 nA. Well-characterized natural and synthetic materials were used as standards for calibration. A ZAF intensity correction routine, and a MAN background intensity correction were applied (see Appendix S1 for details on the technique). The Zr detection limit using this setup is 12 ppm.

Zr-in-rutile temperatures were calculated using the pressure-dependent calibration of Tomkins, Powell, and Ellis (2007), and reported errors are one-sigma. Results are shown in Table 3, and individual analyses for each sample are shown in Table S4.

TABLE 3 Trace element concentrations and calculated temperatures of rutiles from eclogites from the Dulan area, China

		Zr concentration (ppm)				T^b (°C)	
Sample	n^a	Max.	Min.	Average	1σ	Average	1σ
D161B	28	139	55	96	20	638	16
D167	33	205	122	149	17	673	9
D197	54	250	173	206	18	700	7
D205	40	155	113	135	9	666	5

[a]Number of analyses after excluding outliers and rejected analyses (see text).
[b]Temperatures calculated at 30 kbar following the calibration of Tomkins et al. (2007).

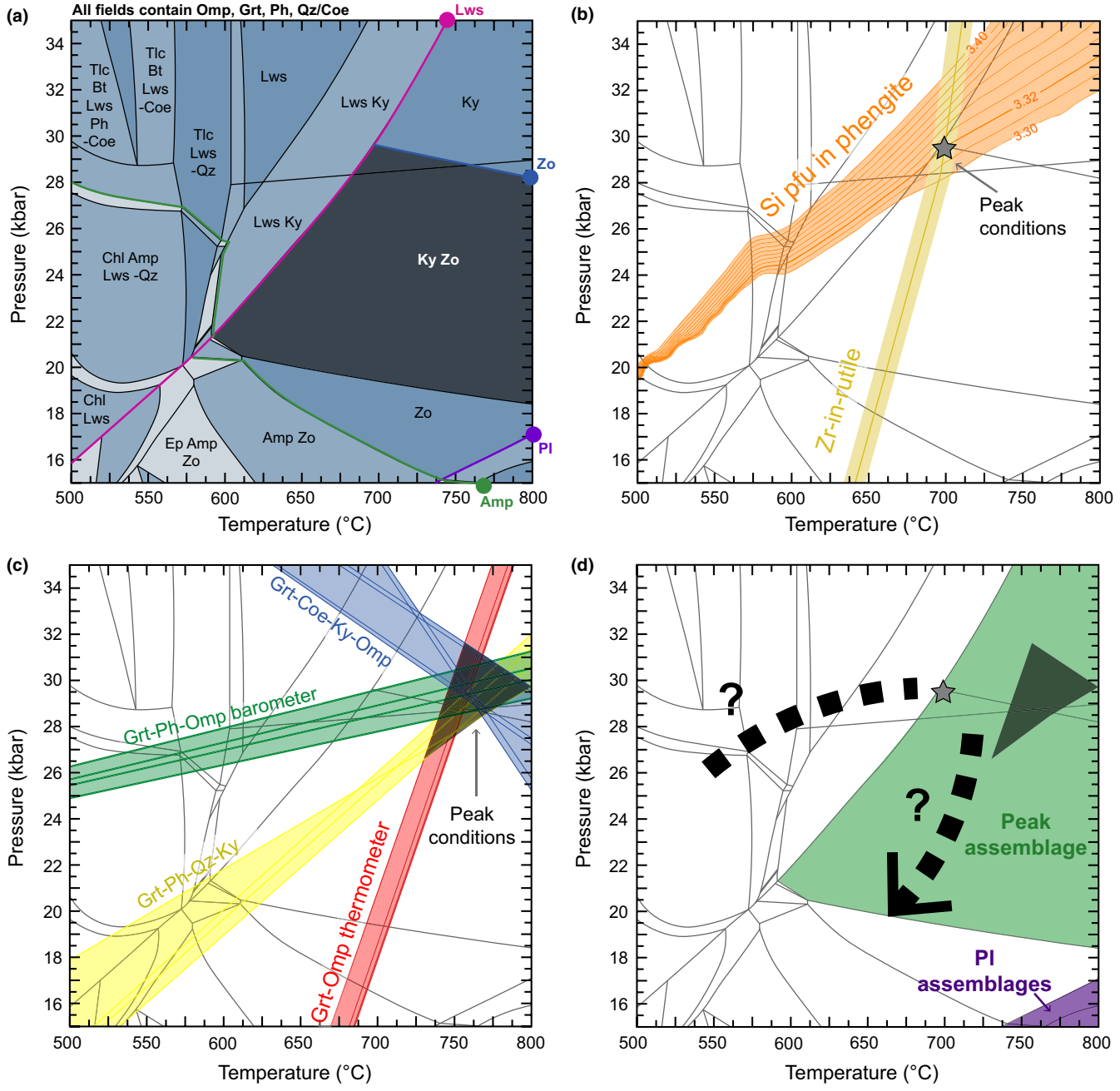

FIGURE 7 Eclogite D197 thermobarometry. (a) Phase equilibrium diagram. The peak assemblage is indicated by the shaded grey area. (b) Peak conditions obtained using the Zr-in-rutile thermometer (±1σ error), and maximum Si pfu in phengite. (c) Peak conditions obtained using garnet–omphacite–kyanite–phengite–coesite/quartz equilibrium (Krogh Ravna, 2000; Krogh Ravna & Terry, 2004). The figure shows all possible combinations of mineral compositions (Table S3). (d) Summary of the *P–T* constraints. Mineral assemblage constraints are shown in different shaded areas. The grey star and grey polygon correspond to those in (b) and (c) respectively

4.2 | Results

4.2.1 | Phengite–zoisite–kyanite eclogite D197

The peak mineral assemblage of eclogite D197 is Grt+Omp+Ph+Ky+Rt+Zo+Qz/Coe. Omphacite and zoisite contain quartz pseudomorphs after coesite (Figure 4a), indicating that they were stable at UHP conditions. The phase equilibrium diagram constructed for the XRF whole-rock composition fails to predict zoisite at UHP conditions, inconsistent with our petrographic observation of quartz pseudomorphs after coesite in the zoisite. Therefore, a reconstructed bulk composition was used to build the phase diagram. The reconstructed bulk composition is significantly higher in Al_2O_3 wt % due to the abundance of kyanite in the thin section compared with the part of the sample

analysed by XRF. Zoning in garnet (Figure 3a) appears to be modified from original growth zoning (see discussion below). Furthermore, phase equilibrium modelling fails to predict the prograde *P–T* path using the intersections between the Grs and Prp isopleths (Figure S3).

The phase equilibrium diagram for eclogite D197 shows that the observed peak assemblage is stable in a large field from >580°C and ~18–30 kbar (Figure 7a). The peak assemblage extends into both the coesite and quartz stability fields. The peak temperature is constrained using the average Zr content of rutile from the sample (Table 3). The Zr-in-rutile isopleth intersects with the maximum phengite Si pfu (Table 1) at ~700°C and ~29 kbar (Figure 7b). The calculated peak conditions are in the field of the observed mineral assemblage. Garnet–omphacite–kyanite–phengite–coesite/quartz equilibrium yields ~725–800°C and ~26–32 kbar (Figure 7c). These conditions overlap the observed assemblage field, and the Ph+Grt+Omp+Ky+Coe/Qz field.

4.2.2 | Phengite eclogite D205

The peak mineral assemblage for sample D205 is Grt+Omp+Ph+Rt+Qz/Coe. Amphibole and epidote porphyroblasts are texturally late and are interpreted to represent retrograde phases. The grossular and pyrope contours from the garnet core (point a in Figure 3b) intersect at ~560°C and ~26 kbar in the Tlc+Ph+Grt+Bt+Omp+Lws field (Figure S4). There are no possible intersections within the *P–T* diagram that can reproduce the observed zoning in the garnet′s mantle and rim (Figure 3b and Figure S4). Therefore, a reliable *P–T* path cannot be calculated using the garnet zoning.

The phase equilibrium diagram shows that the peak assemblage is stable at >620°C and >16 kbar (Figure 8a). The peak assemblage extends into both the coesite and quartz stability fields. The peak temperature is constrained using the average Zr content of rutile from the sample (Table 3). The Zr-in-rutile isopleth intersects with the maximum Si pfu in phengite (Table 1) at ~660°C and ~29 kbar (Figure 8b). These conditions are within the peak assemblage stability field. Garnet–omphacite–phengite thermobarometry yields ~735–763°C and ~35–37 kbar (Figure 8c). These conditions overlap the peak assemblage field.

The retrograde evolution of this eclogite is characterized by the presence of amphibole and epidote poikiloblasts. The assemblage field containing both minerals combined with the isopleth of observed amphibole volume, ~10–15%, delimits the retrograde path to ~590–650°C and ~17–21 kbar (Figure 8a,d). The phase equilibrium diagram predicts that amphibole is the first mineral to form during decompression followed by epidote.

4.2.3 | Phengite eclogite D167

The peak mineral assemblage of eclogite D167 is Grt+Omp+Ph+Rt+Qz/Coe. Omphacite preserves quartz pseudomorphs after coesite, suggesting that it was stable at UHP conditions (Figure 4b). Amphibole and epidote are interpreted as retrograde phases. Phase equilibrium modelling was performed using both XRF and reconstructed whole-rock compositions; however, only the results from the latter are presented here (see discussion). Similar to the samples described above, phase equilibrium modelling fails to predict the prograde *P–T* path using the intersections between the grossular and pyrope isopleths (Figure 3c and Figure S5).

The phase equilibrium diagram for sample D167 reveals that the peak assemblage is stable at >650°C and >22 kbar (Figure 9a). The peak assemblage extends into both the coesite and quartz stability fields. The peak temperature is constrained using the average Zr content of rutile from the sample (Table 3). The Zr-in-rutile isopleth intersects with the maximum Si pfu in phengite (Table 1) at ~675°C and ~32 kbar (Figure 9b). The peak conditions are within the Ph+Grt+Omp+Lws+Coe stability field, close to the boundary of the peak assemblage stability field. Garnet-omphacite-phengite thermobarometry yields ~700–715°C and ~31–32 kbar (Figure 9c). These conditions overlap the peak assemblage stability field.

Constraints on the retrograde history are provided by the presence of amphibole and epidote. The assemblage field containing both minerals combined with the isopleth of observed amphibole volume, ~5–10%, delimits the retrograde path to ~570–770°C and ~15–22 kbar (Figure 9a,d). The phase equilibrium diagram predicts that epidote is the first mineral to form during decompression followed by amphibole.

4.2.4 | Phengite eclogite D161B

The peak mineral assemblage for eclogite D161B is Grt+Omp+Ph+Rt+Qz/Coe. Zoisite and amphibole porphyroblasts (Figure 2g) are interpreted to represent retrograde phases. Epidote and amphibole elongated inclusions, commonly multiphase (Figure 2h), are interpreted as lawsonite pseudomorphs (see discussion). The hand sample shows strong compositional banding, and the phase equilibrium diagram built with the XRF whole-rock data fails to predict the complete observed assemblage. Therefore, a reconstructed bulk composition was used to build the phase diagram. Similar to the samples described above, phase equilibrium modelling fails to predict the prograde *P–T* path using the intersections between the Grs and Prp isopleths (Figure 6 and Figure S6).

The phase equilibrium diagram shows that the peak assemblage is stable at >610°C and >16 kbar (Figure 10a).

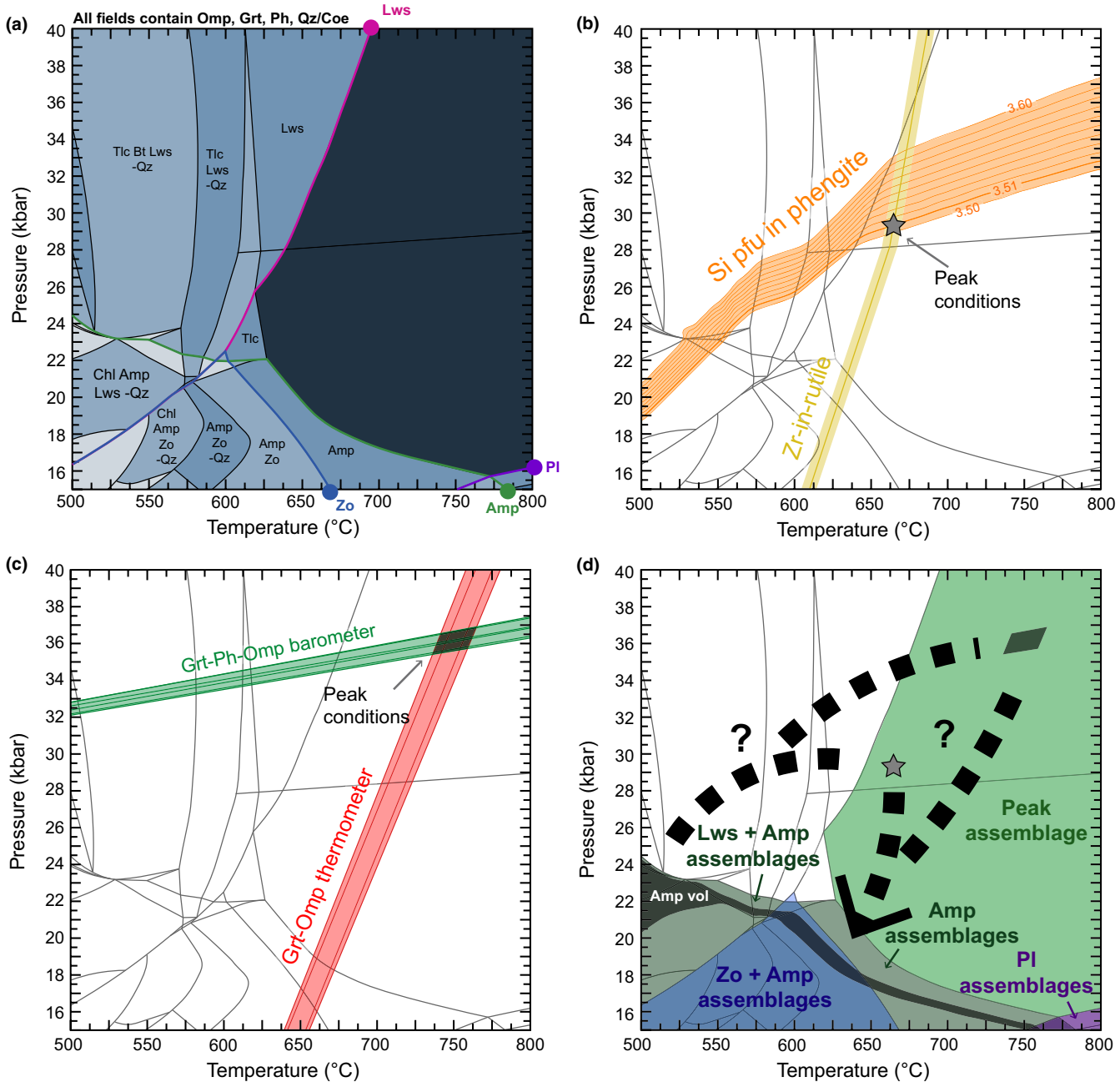

FIGURE 8 Eclogite D205 thermobarometry. (a) Phase equilibrium diagram. The peak assemblage is indicated by the shaded grey area. (b) Peak conditions obtained using the Zr-in-rutile thermometer (±1σ error), and maximum Si pfu in phengite. (c) Peak conditions obtained using garnet–omphacite–phengite thermobarometry (Krogh Ravna, 2000; Krogh Ravna & Terry, 2004). The figure shows all possible combinations of mineral compositions (Table S3). (d) Summary of the *P*–*T* constraints. The retrograde conditions are constrained by the observed amphibole volume (10–15%). Mineral assemblage constraints are shown in different shaded areas. The grey star and grey polygon correspond to those in b and c respectively

The peak assemblage extends into both the coesite and quartz stability fields. The peak temperature is constrained using the average Zr content of rutile from the sample (Table 3). The Zr-in-rutile isopleth intersects with the maximum Si pfu in phengite (Table 1) at ~625°C and ~26 kbar (Figure 10b). These conditions are within the Ph+Grt+Omp+Lws+Qz stability field, close to the boundary of the peak assemblage field.

Garnet–omphacite–phengite thermobarometry yields ~600–660°C and ~24–25 kbar (Figure 10c). These conditions overlap the peak assemblage field, Ph+Grt+Omp+Lws+Qz, and the Tlc+Ph+Grt+Omp+Lws+Qz stability field.

The prograde *P*–*T* path for eclogite D161B was determined by modelling garnet growth using the intersections between garnet grossular and volume isopleths, calculated

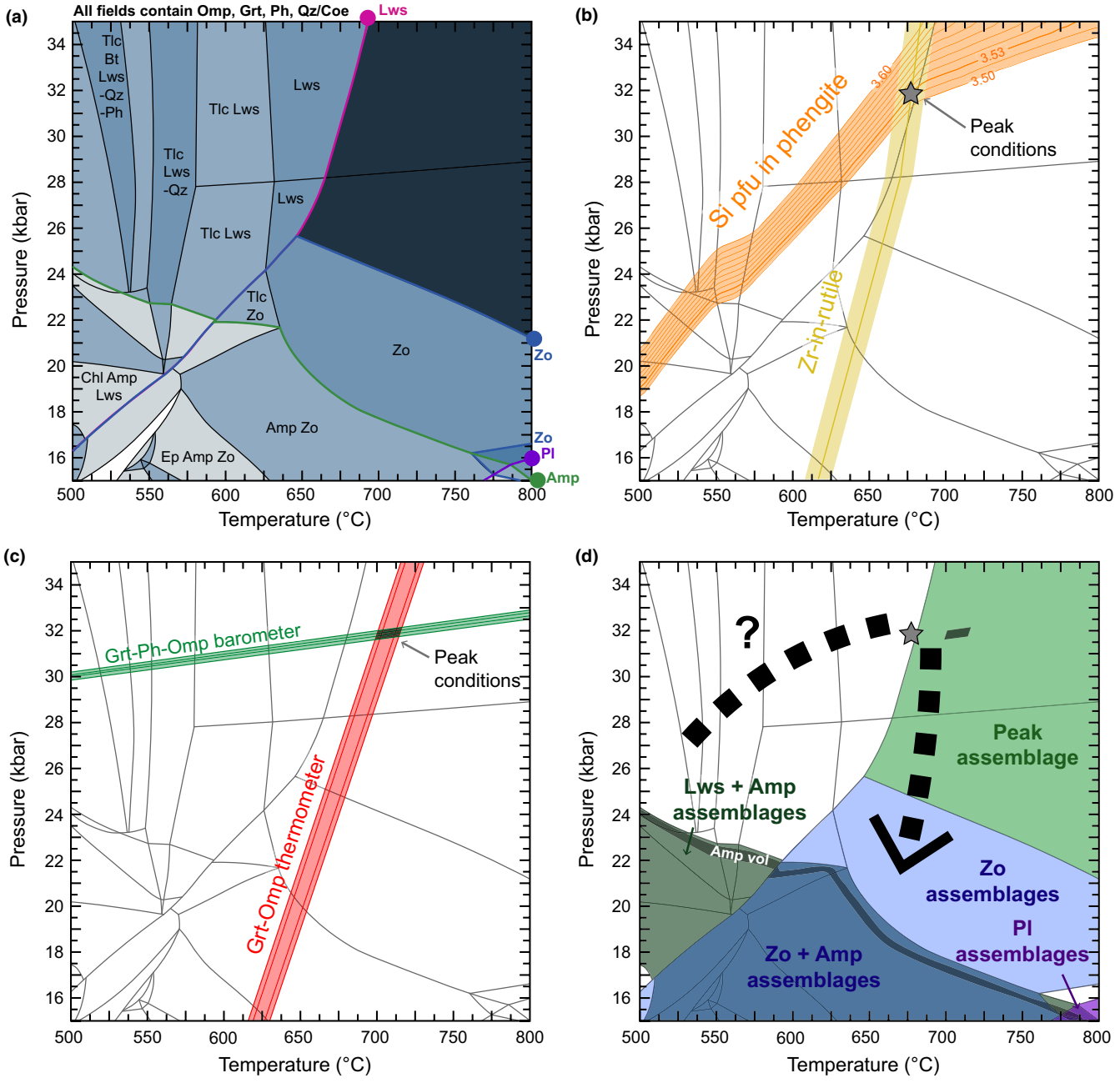

FIGURE 9 Eclogite D167 thermobarometry. (a) Phase equilibrium diagram. The peak assemblage is indicated by the shaded grey area. (b) Peak conditions obtained using the Zr-in-rutile thermometer (±1σ error), and maximum Si pfu in phengite. (c) Peak conditions obtained using garnet–omphacite–phengite thermobarometry (Krogh Ravna, 2000; Krogh Ravna & Terry, 2004). The figure shows all possible combinations of mineral compositions (Table S3). (d) Summary of the *P–T* constraints. The retrograde conditions are constrained by the observed amphibole volume (5–10%). Mineral assemblage constraints are shown in different shaded areas. The grey star and grey polygon correspond to those in b and c respectively

from the 29 points of the garnet compositional profile (Figures 6 and 11; Table S2). The phase equilibrium diagram reveals that the garnet volume increase as *P–T* increases, garnet volume isopleths are closely spaced in a temperature range of 500–600°C, and as the volume isopleths get to the Ph+Grt+Omp+Qz/Coe field, they become more widely spaced (Figure 11a). Garnet volume isopleths are strongly temperature dependent in the lawsonite stability field, whereas in the zoisite field, volume isopleths have a gentle negative slope (Figure 11a). Grossular content generally decreases as *P–T* increases, but in the Ph+Grt+Omp+Qz/Coe field, grossular slightly increases with *P–T* (Figure 11b). The *P–T* point where the first garnet crystalizes lies outside the *P–T* range of the diagram, so the prograde *P–T* path begins at ~410°C and ~17 kbar, with a garnet volume of ~1% and a value of ~35% Grs

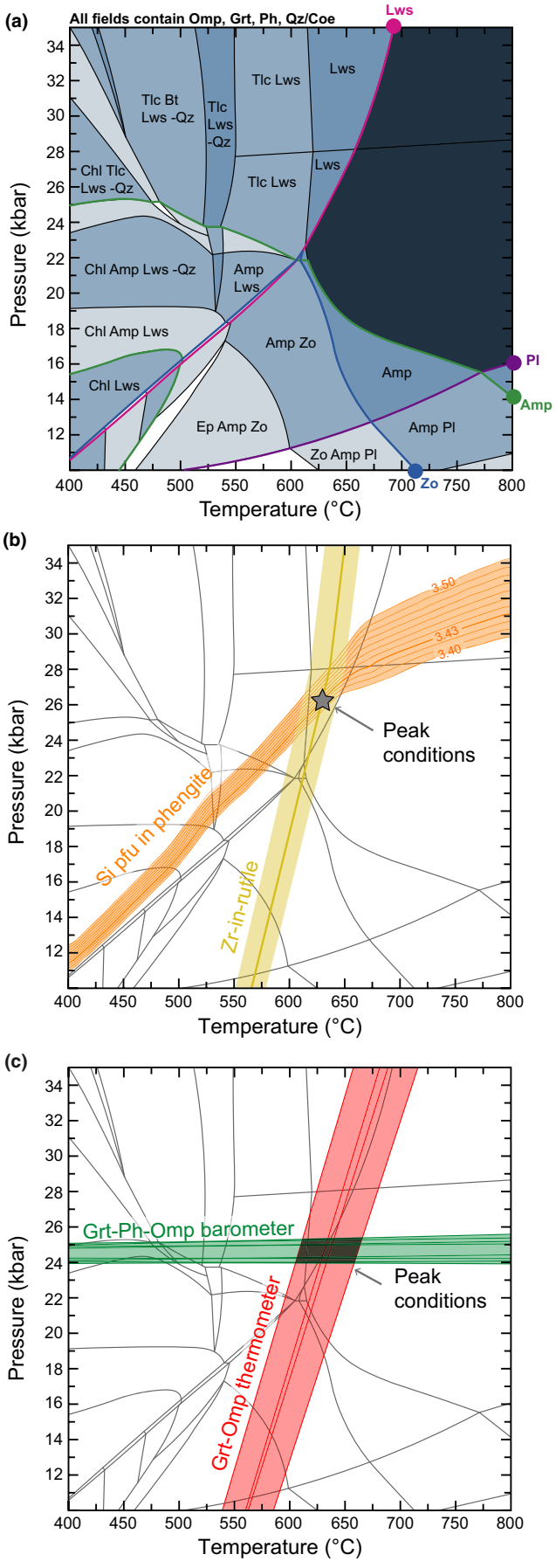

FIGURE 10 Eclogite D161B thermobarometry. (a) Phase equilibrium diagram. The peak assemblage is indicated in the shaded grey area. (b) Peak conditions obtained using the Zr-in-rutile thermometer (±1σ error), and maximum Si pfu in phengite. (c) Peak conditions obtained using garnet–omphacite–phengite thermobarometry (Krogh Ravna, 2000; Krogh Ravna & Terry, 2004). The figure shows all possible combinations of mineral compositions (Table S3)

(point 1 in Figure 11c; Table S2). These conditions are in the Chl+Amp+Ph+Grt+Omp+Lws+Qz stability field. Garnet growth continues to the mantle composition at ~540°C and ~28 kbar, with a garnet volume of ~18% and a value of ~25% Grs (point 15 in Figure 11c; Table S2). These conditions are in the Tlc+Ph+Grt+Omp+Lws stability field. Then, the model predicts a pressure reversal to ~550°C and ~26 kbar, with a garnet volume of ~18% and a value of ~28% Grs (point 16 in Figure 11c; Table S2). These conditions are in the Tlc+Ph+Grt+Omp+Lws+Qz stability field. According to our *P–T* path, the garnet rim forms at ~625°C and ~35 kbar. These conditions correspond to a garnet volume of 30% and a Grs of 22% (point 29 in Figure 11c; Table S2). These conditions are in the Ph+Grt+Omp+Lws+Coe stability field.

The retrograde evolution of this eclogite is characterized by the presence of amphibole and zoisite. The assemblage field containing both minerals combined with the isopleth of observed amphibole mode, ~10–15%, delimits the retrograde path to ~590–640°C and ~17–21 kbar (Figures 10a and 11c). The phase equilibrium diagram predicts that the first mineral to form during decompression is amphibole followed by zoisite (Figures 10a and 11c).

5 | DISCUSSION AND CONCLUSIONS

5.1 | Metamorphism of the Dulan area, North Qaidam UHP terrane

5.1.1 | Prograde metamorphism

Eclogite D161B followed a *P–T* path through a gradient of 5–9°C/km, typical of subduction zones (Figures 11c and 12; Penniston-Dorland, Kohn, & Manning, 2015; Syracuse, van Keken, & Abers, 2010). The obtained prograde *P–T* path indicates a clockwise trajectory, and that the eclogite evolves through the lawsonite stability field (Figures 11c and 12), similar to *P–T* paths of UHP eclogites in the Dabieshan, China (e.g., Wei, Cui, & Tian, 2015; Wei, Li, Yu, & Zhang, 2010), and Tso Morari, India (e.g., Palin, Reuber, White, Kaus, & Weller, 2017; St-Onge et al., 2013).

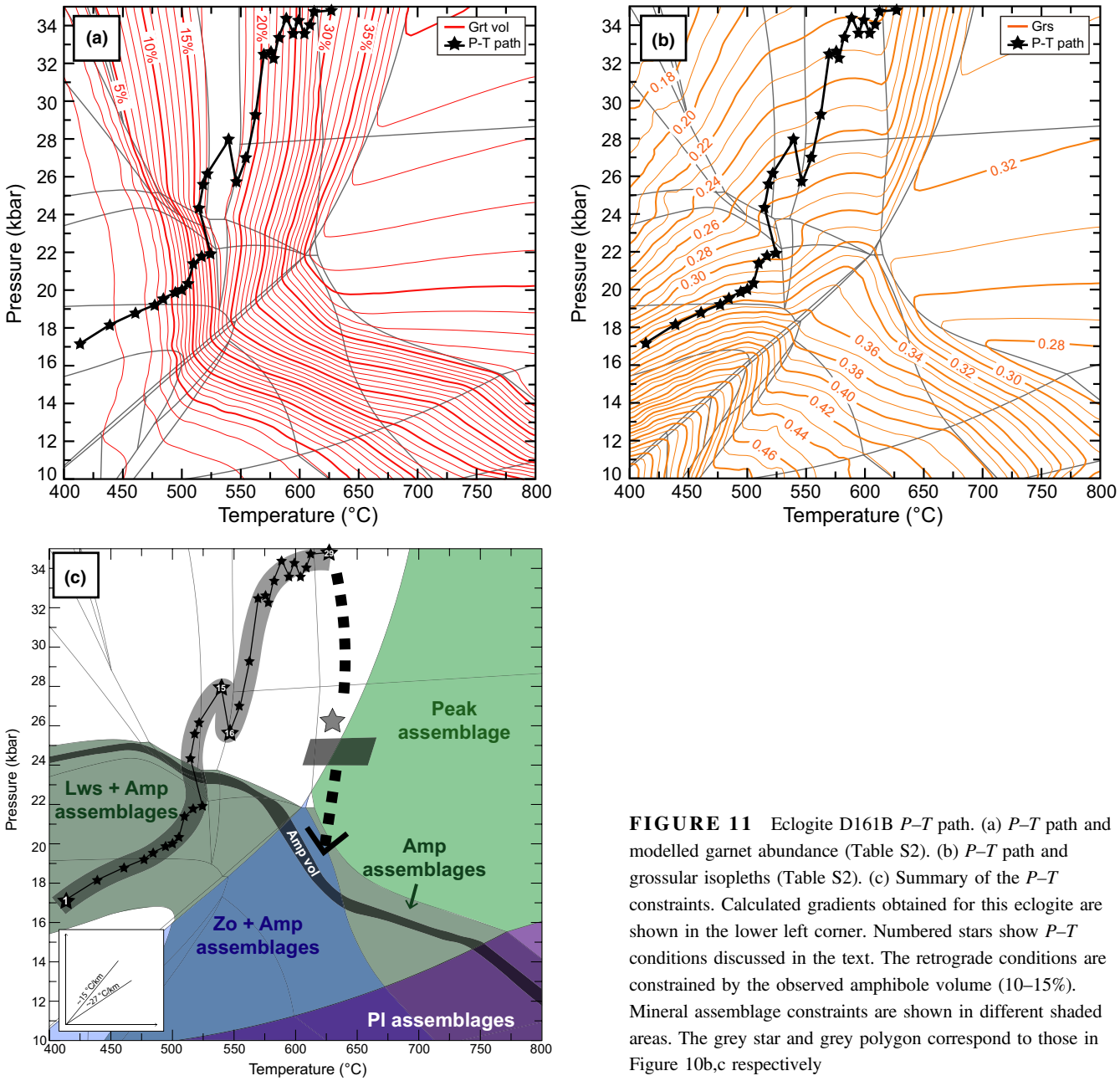

FIGURE 11 Eclogite D161B *P–T* path. (a) *P–T* path and modelled garnet abundance (Table S2). (b) *P–T* path and grossular isopleths (Table S2). (c) Summary of the *P–T* constraints. Calculated gradients obtained for this eclogite are shown in the lower left corner. Numbered stars show *P–T* conditions discussed in the text. The retrograde conditions are constrained by the observed amphibole volume (10–15%). Mineral assemblage constraints are shown in different shaded areas. The grey star and grey polygon correspond to those in Figure 10b,c respectively

Our *P–T* path of the Dulan eclogites contrasts with the nearly isothermal prograde *P–T* path from ~10 to ~30 kbar proposed by Ren et al. (2016) and Zhang, Ellis, et al. (2010) (Figure 12). On the other hand, our results are in good agreement with the presence of polycrystalline blocky-shaped epidote-amphibole inclusions in garnet from eclogites of the Dulan area, interpreted as pseudomorphs after lawsonite (Mattinson et al., 2006). Multiphase inclusions in D161B garnet contain the same epidote–amphibole assemblage, suggesting that they also are products of lawsonite breakdown even though the blocky morphology is not developed. The lack of lawsonite, and the ubiquitous presence of zoisite and amphibole in the eclogites suggest that the exhumation path for the Dulan area was not suitable for the preservation of lawsonite (see discussion below; Clarke, Powell, & Fitzherbert, 2006; Tsujimori, Sisson, Liou, Harlow, & Sorensen, 2006; Wei & Clarke, 2011; Wei & Tian, 2014; Wei, Yang, Su, Song, & Zhang, 2009; Whitney & Davis, 2006; Zack, Rivers, Brumm, & Kronz, 2004).

The *P–T* path shows an apparent pressure drop (~3 kbar) during the prograde burial at ~545°C (Figure 11). This reversal is a consequence of the increase in Ca in the garnet mantle, which appears to be a common feature in Dulan UHP eclogites (Figure 6 and Figure S2; Meyer, Mattinson, & Zhang, 2015). The apparent pressure reversal might reflect one or more of the following: (a) a major tectonic event. Published studies suggest that oscillatory zoning in

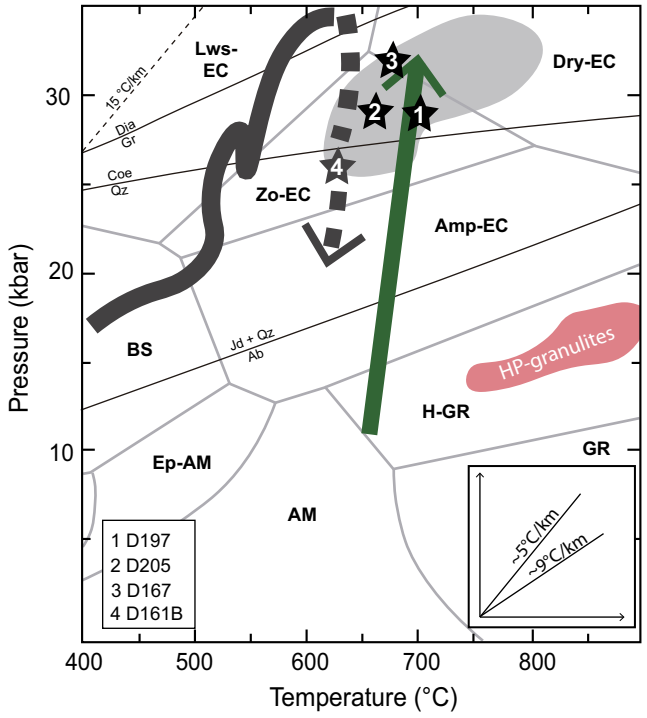

FIGURE 12 Summary of the *P–T* constraints from Dulan eclogites. The green line depicts the proposed prograde *P–T* path of Ren et al. (2016) and Zhang, Ellis, et al. (2010). The red area corresponds to the *P–T* conditions for the HP granulites (Yu et al., 2011, 2014). The grey area represents previous *P–T* estimates using conventional thermobarometry for eclogites of the Dulan area (Ren et al., 2016; Song et al., 2003; Zhang, Ellis, et al., 2010; Zhang, Mattinson, et al., 2010; Zhang, Meng, et al., 2009; Zhang, Zhang, et al., 2009). Metamorphic facies and abbreviations follow Liou, Tsujimori, Zhang, Katayama, and Maruyama (2004)

minerals can reflect burial and exhumation cycles (e.g., García-Casco, Torres-Roldán, Millán, Monié, & Schneider, 2002; Rubatto et al., 2011). Our phase equilibrium diagrams suggest a decompression event (~9 km); and/or (b) a disequilibrium and/or kinetic effect. The lack of correlation between the garnet Ca zoning with Fe, Mg, and Mn suggests that Ca might have been transport controlled (Chernoff & Carlson, 1997; García-Casco et al., 2002; Konrad-Schmolke et al., 2005; Spear & Daniel, 2001). However, because diffusion might have affected the rock at peak conditions (see discussion below), the lack of zoning correlation (i.e., Ca with respect Fe, Mg, and Mn) might not be indicative of this process. A change in the kinetics of crystal growth could also influence the zoning (Kohn, 2004; Pattison & Tinkham, 2009; Stowell, Zuluaga, Boyle, & Bulman, 2011). As shown in Figure 11a,b, once the sample crosses the 5% garnet volume isopleth, the garnet growth rate is predicted to increase until it reaches the 17% volume isopleth where chlorite leaves the assemblage and the garnet growth rate is predicted to sharply decrease (i.e., in the Tlc+Ph+Grt+Omp+Lws stability field), and then increase again once it crosses the 18% volume isopleth (i.e., when enters to the Tlc+Ph+Grt+Omp+Lws+Qz stability field). The increase in Ca in the garnet mantle occurs when the garnet growth rate is predicted to change from slow to rapid, suggesting that the Ca oscillation could be a consequence of the change of growth rate; and/or (c) episodic Ca release due to break down of Ca-bearing minerals at this stage (e.g., apatite or carbonates; Indares, White, & Powell, 2008; Groppo, Rolfo, & Indares, 2012); and/or (d) fluid–rock interaction. Garnet growth and resorption events might be triggered by fluid pulses (Ague & Axler, 2016; Faryad, Klápová, & Nosál, 2010; Giuntoli et al., 2018). As recently suggested by Viete et al. (2018), these fluid pulses might induce overpressure cycles (drained and undrained conditions), causing pressure fluctuations without changes in depth.

Given that the phase equilibrium diagram is a simplified qualitative model of a natural process, it is also possible that the apparent pressure reversal is a result of the uncertainties related to the modelling, but the general trend of the *P–T* path should be reliable (de Capitani & Petrakakis, 2010; Powell & Holland, 2008).

5.1.2 | Peak conditions

Eclogites from the southern part of the Dulan area yield peak conditions of ~700°C and ~29 kbar for eclogite D197, ~660°C and ~29 kbar for eclogite D205, and ~625°C and ~26 kbar for eclogite D161B (Figure 12). Eclogite D167 from the north part of the Dulan area yields ~675°C and ~32 kbar (Figure 12). These conditions are in the Grt+Omp+Ph+Rt+Qz/Coe±Ky±Zo stability field, with the exception of eclogites D161B and D167, where the peak conditions are obtained in the lawsonite stability field. Eclogite D161B yields the lowest temperatures conditions of our sample set, agreeing with the preservation of the strongest compositional zoning of all our samples, similar to the temperature–zoning relations of different types of eclogites in the Western Gneiss Region, Norway (e.g. Carswell & Cuthbert, 2003; Cuthbert, Carswell, Krogh-Ravna, & Wain, 2000).

Our *P–T* constraints have a significantly narrower range than those previously obtained with conventional thermometry (Ren et al., 2016; Song et al., 2003, 2006, 2014; Zhang, Ellis, et al., 2010; Zhang, Meng, et al., 2009; Zhang, Mattinson, et al., 2010; Zhang, Zhang, et al., 2009), and indicate that the southern and northern part of the Dulan area experienced the same peak conditions (Figure 12). Diffusional modification of garnet (see discussion below) might partially account for the scattered *P–T* conditions from conventional thermobarometry in previous work.

For all eclogite samples, the peak conditions obtained using the phengite–rutile approach yield *P–T* conditions in

the coesite stability field (Figure 12), with the exception for eclogite D161B (Figure 12). The peak *P–T* conditions obtained from all the eclogites imply depths of ~80–100 km, and are consistent with the petrographic observation of quartz pseudomorphs after coesite in zoisite and omphacite reported in this study (Figure 4), and coesite inclusions in garnet and omphacite reported in the area (Figure 1; Zhang, Mattinson, et al., 2010; Zhang, Meng, et al., 2009; Zhang, Zhang, et al., 2009).

Peak *P–T* estimates of all our samples fall close to the limit of the lawsonite stability field (Figures 7d, 8d, 9d, and 11c). Fluid release associated with lawsonite breakdown is expected to be a main source of fluids at eclogite facies conditions (Groppo & Castelli, 2010; Kerrick & Connolly, 2001; Peacock, 1993). These fluids can re-equilibrate mineral compositions, and therefore, the *P–T* conditions recorded by phengite and rutile may record the *P–T* point where lawsonite breakdown liberated fluids rather than the maximum pressure of the *P–T* path (Figure 11c; Wei, Qian, & Tian, 2013; Wei et al., 2009), supported by our results.

5.1.3 | Retrograde metamorphism

The lack of connection between the last point of the D161B calculated *P–T* path (i.e., point 29 in Figure 11c), and the peak conditions constrained using the phengite-rutile approach (grey star in Figure 11c) might reflect resorption of garnet during exhumation, supported by the observation of resorption surface 2 (Figure S2). This process would consume the garnet that would have resulted in points along the missing space between the obtained peak conditions and the modelled *P–T* path (e.g., Groppo et al., 2015; O'Brien, 1997). The black box in Figure 6 shows garnet overgrowth with a composition similar to the expected composition for the missing *P–T* path (Figure 11b). Furthermore, the resorption event might have been enhanced by fluid pulses (see below), similar to the prograde path (Giuntoli et al., 2018).

Textural relations suggest that epidote and amphibole in samples D205, D167, and D161B crystallized during retrogression. We interpret the formation of these minerals to be compelling evidence of fluid infiltration at early-retrograde conditions (Figures 8d, 9d, and 11c). Dehydration of hydrous minerals, such as lawsonite and talc, liberate large amounts of fluids that can hydrate surrounding UHP rocks in the subduction zone (Clarke et al., 2006; de Sigoyer, Guillot, Lardeaux, & Mascle, 1997; Massonne, 2012; Palin, St-Onge, Waters, Searle, & Dyck, 2014; Pawley, 1994; Schmidt, 1995; Wei & Clarke, 2011; Wei et al., 2009). Fluids related to lawsonite or talc breakdown in eclogites at greater depths in the subduction zone can be responsible for hydrating eclogite facies assemblages in rocks located at lower depths, triggering the growth of hydrous minerals, such as amphibole and epidote at depths of ~60 km.

Amphibole compositional zoning is expected to evolve to glaucophane if the retrograde *P–T* path experiences significant cooling, however, the observed amphibole zoning in eclogite D205 (calcic cores to sodic-calcic rims; Figure S1 and Table S1) indicate that the eclogite experienced high enough temperatures during exhumation to be in the calcic amphibole stability field (e.g., Forneris & Holloway, 2003; Weller, Wallis, Aoya, & Nagaya, 2015; Wei et al., 2013; Wilke, O'Brien, & Altenberger, 2010). Our results indicate that the Dulan eclogites experienced a retrograde *P–T* path to temperatures of ~580–660°C, enough to obliterate any evidence of lawsonite, but cold enough to preclude partial melting (Figures 8d, 9d, and 11c; Clarke et al., 2006; Wei & Clarke, 2011). These results contrast with the hypothesis that eclogites from the south part of the Dulan area experienced wide-spread granulite facies conditions during exhumation (Ren et al., 2016; Song et al., 2003, 2014; Zhang et al., 2015). Furthermore, phengite in metabasic rocks is expected to disappear on the solidus (Schmidt & Poli, 1994; Schmidt, Vielzeuf, & Auzanneau, 2004); the presence of this mineral in the eclogites from the southern part of the Dulan area is inconsistent with the idea that these eclogites experienced retrogression to granulite facies conditions and partial melting.

5.2 | Implications for thermobarometry of MT–UHP eclogites

5.2.1 | Whole-rock composition

Our results indicate that, even though MT–UHP eclogites present relatively simple mineral assemblages, compositional heterogeneities can affect the results of phase equilibrium modelling. A good example is eclogite D197, where the phase equilibrium diagram calculated for the modified XRF data fails to predict the observed mineral assemblage. Our results suggest that it is important to compare XRF and reconstructed bulk compositions because, even if the compositional heterogeneities are not a disequilibrium feature, they can have important effects in the topology of the phase equilibrium diagram (Guevara & Caddick, 2016; Lanari & Engi, 2017; Palin et al., 2016). For instance, we calculated phase equilibrium diagrams for eclogite D167 using both XRF data (Figure S7) and a reconstructed bulk composition (Figure 9). The phase equilibrium modelling using both compositions yields relatively similar peak *P–T* conditions (±3 kbar), but the lawsonite stability fields shifted to higher temperatures, and the zoisite stability fields shifted to higher pressures in the phase equilibrium diagram built using the reconstructed bulk composition (Figure 9 and Figure S7). As a result, the peak

conditions lie very close to the limit of the lawsonite stability field for the diagram calculated using the reconstructed bulk composition, similar to results for the other samples and consistent with the hypothesis that phengite–rutile *P–T* conditions reflect fluid release and re-equilibration due to lawsonite breakdown. The diagram calculated for the reconstructed bulk composition is our preferred result because this approach is expected to better reproduce the observations made at the thin section scale, although this technique might introduce biases, such as point-counting mis-estimations related to geological uncertainties (cf. Palin et al., 2016).

5.2.2 | Garnet diffusion: complexities of phase equilibrium modelling

Our results demonstrate that modelling of garnet zoning using the compositional isopleth approach (i.e., intersection between multiple compositional isopleths) is not suitable for building complete *P–T* paths for the studied eclogites (Figures S3–S6). The observed zoning of X_{Mg}, Alm, and Prp (Figures 3 and 6) is not predicted by the phase equilibrium diagrams (Figures S3–S6). The garnet X_{Mg} in eclogites D167 and D205 shows a subtler increase from core to rim than expected, whereas in eclogite D197, the X_{Mg} is nearly homogenous through the garnet (Figure 3). This suggests that diffusion of Fe and Mg has modified the original garnet composition, changing X_{Mg} and producing the observed patterns (Caddick et al., 2010; Carlson, 2006; Konrad-Schmolke, O'Brien, de Capitani, & Carswell, 2008; Konrad-Schmolke et al., 2005; Štípská & Powell, 2005). Other evidence that diffusion affected garnet is the presence of low-Mg patchy zones (that might be closer to the original garnet core composition) found in garnet from eclogite D161B (Figure 6). With the exception of sample D161B, garnet zoning in the samples is weak and uncommon. Figures 3 and 6 show examples of the strongest zoning found in the studied eclogites. The lack of wide-spread zoning suggests that most of the eclogites re-equilibrated, obscuring prograde *P–T* conditions (Caddick et al., 2010; Konrad-Schmolke et al., 2005, 2008). The long HP–UHP event experienced by the Dulan area at moderate peak temperatures (Mattinson et al., 2006) might have facilitated the compositional modification off garnet.

Even though eclogite D161B displays Prp and X_{Mg} zoning (Figure 6), the zoning is less than expected (Figure S6), suggesting diffusional modification and questioning the reliability of using the pyrope and almandine isopleths for *P–T* path determination (Figure S6). For instance, without diffusional modification, garnet is predicted to show a stronger increase of Alm (0.22–0.62), Prp (0.01–0.26), and X_{Mg} (0.05–0.35), and a stronger decrease of Sps (0.42–0.01) from core to rim compared to the observed zoning (Figure S6e). By contrast, the preservation of fine-scale features in Ca zoning suggests that Ca zoning is more likely to represent the original garnet composition, consistent with the low diffusion rate of Ca compared to Fe and Mg (Carlson, 2006; Carlson et al., 2015; Chakraborty & Ganguly, 1992; Chernoff & Carlson, 1997; Florence & Spear, 1991; Giuntoli et al., 2018). Therefore, the *P–T* path constructed for eclogite D161B using the garnet volume and the Grs content should represent a valid constraint.

5.2.3 | Conventional thermobarometry versus phase equilibrium modelling

Peak conditions calculated with conventional thermobarometry are within ~3 kbar and ~50°C of the conditions obtained using the phengite–rutile approach (Figures 7d, 9d, and 11c), with the exception of eclogite D205, where conventional thermobarometry yields substantially higher *P–T* conditions (Figure 8d). As has been widely discussed (e.g., Carswell, O'Brien, Wilson, & Zhai, 1997; Hacker, 2006; Krogh Ravna & Terry, 2004; Powell & Holland, 2008), there are large uncertainties associated with the garnet-omphacite thermometer associated with Fe^{3+} in omphacite. We interpret the peak conditions obtained using the phengite–rutile approach to be more reliable because it is less sensitive to uncertainties associated with ferric iron compared to conventional thermobarometry. Furthermore, complementing phase equilibrium modelling (e.g., Si pfu in phengite isopleths) with independent thermometry (e.g., Zr-in-rutile thermometry) appears to be a robust way to obtain peak *P–T* conditions because the thermometry is independent of the data and assumptions made in phase equilibrium modelling (e.g., Powell & Holland, 2008; Štípská & Powell, 2005; Wei & Clarke, 2011). Therefore, our discussion of the peak conditions of the Dulan area is made using the results obtained with phengite–rutile approach.

5.2.4 | Sensitivity of conventional thermobarometry results

As mentioned above, conventional thermobarometry of eclogite D205 yields substantially higher *P–T* conditions than using the phengite–rutile approach (Figure 8d). According to the calibration of the conventional thermobarometry used in this paper, the highest $Grs^2 \times Prp$ garnet value will yield the highest *P–T* conditions (Krogh Ravna & Terry, 2004). A simple test was made in eclogite D205 to evaluate the sensitivity of the conventional *P–T* results as a function of the garnet composition. For this purpose, the highest jadeite content in omphacite and the highest Si pfu in phengite were used as fixed values, and the garnet

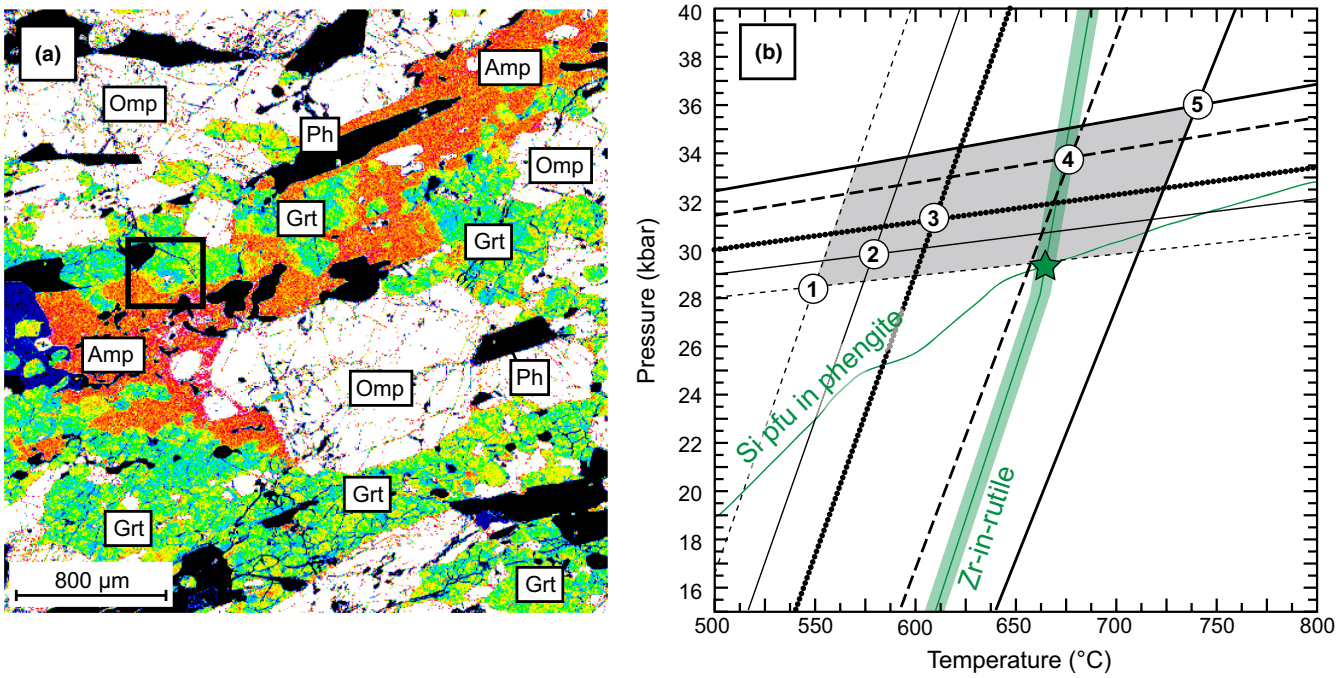

FIGURE 13 Conventional thermobarometry sensitivity test for eclogite D205. (a) $Grs^2 \times Prp$ X-ray map. The garnet in the black box corresponds to the garnet profile in Figure 3b. (b) *P–T* results. Numbers correspond to the mineral combinations shown in Table S6

composition was changed for the *P–T* calculations (Figure 13; Table S5). As shown in Figure 13a, some garnet grains show homogenous $Grs^2 \times Prp$ compositions, and others display irregular $Grs^2 \times Prp$ zoning that we interpret as evidence of compositional modification. Our results show that garnet composition has a strong influence in the obtained *P–T* conditions, yielding a range of values of ~550–745°C and ~28–36 kbar (Figure 13b; Table S6). These results show that the garnet rim values yield the highest *P–T* conditions and the core values yield the lowest *P–T* result, consistent with the increase of $Grs^2 \times Prp$ from core to rim (Table S6). The peak conditions obtained from the phengite–rutile approach are close to the values from the garnet mantle and inner rim (Figure 13b; Table S6). These garnet zones display similar $Grs^2 \times Prp$ composition to that of most garnet at the thin section scale (Figure 13a). Results from the other samples also suggest that the highest $Grs^2 \times Prp$ does not necessarily correspond to the peak conditions reached by the eclogite. For instance, in eclogite D197 and D161B, the lowest $Grs^2 \times Prp$ values belong to the rims (opposite to eclogite D205), and in eclogite D167, the $Grs^2 \times Prp$ zoning is irregular and does not show major changes through the sample (Table 1 and Table S3). These results suggest that the traditional methodology to select mineral compositions for conventional thermobarometry that will yield maximum *P–T* conditions (e.g., Carswell, Wilson, & Zhai, 2000; Krogh Ravna & Terry, 2004) might result in inaccurate conditions if the garnet composition has been modified by diffusion.

ACKNOWLEDGEMENTS

We thank A. Sains, M. Lehman, K. Stubbs, and V. Gilmore for help with EMP and XRF analyses, O. Neill and S. Boroughs for assistance in the Peter Hooper GeoAnalytical Laboratory at Washington State University, and F. Gutiérrez-Aguilar, R. Palin, A. García-Casco, and M. Konrad-Schmolke for insightful comments and discussion. Reviews by C. Groppo, and C.J. Wei greatly improved the manuscript, and are gratefully acknowledged. R. White and D. Robinson are thanked for editorial handling. This study was funded by a Geological Society of America (GSA) graduate student research grant, and GSA Mineralogy Geochemistry Petrology and Volcanology division student research grant to D. Hernández-Uribe, by National Science Foundation grant NSF-EAR1347433 to C.G. Mattinson, and by National Natural Science Foundation of China grant 41630207 to J.X. Zhang.

ORCID

David Hernández-Uribe http://orcid.org/0000-0002-5335-4131
Jianxin Zhang http://orcid.org/0000-0002-5733-8091

REFERENCES

Ague, J. J., & Axler, J. A. (2016). Interface coupled dissolution-reprecipitation in garnet from subducted granulites and ultrahigh-pressure rocks revealed by phosphorous, sodium, and titanium zonation. *American Mineralogist*, *101*(7), 1696–1699. https://doi.org/10.2138/am-2016-5707

Bureau of Geology and Mineral Resources of Qinghai Province. (1968). *Geological map of the Dulan area, 1:200000*. Beijing, China: Geological Publishing House (in Chinese).

Caddick, M. J., Konopásek, J., & Thompson, A. B. (2010). Preservation of garnet growth zoning and the duration of prograde metamorphism. *Journal of Petrology*, *51*(11), 2327–2347. https://doi.org/10.1093/petrology/egq059

de Capitani, C. D., & Petrakakis, K. (2010). The computation of equilibrium assemblage diagrams with Theriak/Domino software. *American Mineralogist*, *95*(7), 1006–1016. https://doi.org/10.2138/am.2010.3354

Carlson, W. D. (2006). Rates of Fe, Mg, Mn, and Ca diffusion in garnet. *American Mineralogist*, *91*(1), 1–11. https://doi.org/10.2138/am.2006.2043

Carlson, W. D., Pattison, D. R. M., & Caddick, M. J. (2015). Beyond the equilibrium paradigm: How consideration of kinetics enhances metamorphic interpretation. *American Mineralogist*, *100*(8–9), 1659–1667. https://doi.org/10.2138/am-2015-5097

Carswell, D. A., & Cuthbert, S. J. (2003). Ultrahigh pressure metamorphism in the Western Gneiss Region of Norway. *EMU Notes in Mineralogy*, *5*, 51–73.

Carswell, D. A., O′Brien, P. J., Wilson, R. N., & Zhai, M. G. (1997). Thermobarometry of phengite–bearing eclogites in the Dabie Mountains of central China. *Journal of Metamorphic Geology*, *15*(2), 239–252. https://doi.org/10.1111/j.1525-1314.1997.00014.x

Carswell, D. A., Wilson, R. N., & Zhai, M. G. (2000). Metamorphic evolution, mineral chemistry and thermobarometry of schists and orthogneisses hosting ultra–high pressure eclogites in the Dabieshan of central China. *Lithos*, *52*(1–4), 121–155. https://doi.org/10.1016/S0024-4937(99)00088-2

Chakraborty, S., & Ganguly, J. (1992). Cation diffusion in aluminosilicate garnets: Experimental determination in spessartine-almandine diffusion couples, evaluation of effective binary diffusion coefficients, and applications. *Contributions to Mineralogy and Petrology*, *111*(1), 74–86. https://doi.org/10.1007/BF00296579

Chernoff, C. B., & Carlson, W. D. (1997). Disequilibrium for Ca during growth of pelitic garnet. *Journal of Metamorphic Geology*, *15*(4), 421–438. https://doi.org/10.1111/j.1525-1314.1997.00026.x

Chopin, C. (2003). Ultrahigh–pressure metamorphism: Tracing continental crust into the mantle. *Earth and Planetary Science Letters*, *212*(1–2), 1–14. https://doi.org/10.1016/S0012-821X(03)00261-9

Clarke, G. L., Powell, R., & Fitzherbert, J. A. (2006). The lawsonite paradox: A comparison of field evidence and mineral equilibria modelling. *Journal of Metamorphic Geology*, *24*(8), 715–725. https://doi.org/10.1111/j.1525-1314.2006.00664.x

Coggon, R., & Holland, T. J. B. (2002). Mixing properties of phengitic micas and revised garnet–phengite thermobarometers. *Journal of Metamorphic Geology*, *20*(7), 683–696. https://doi.org/10.1046/j.1525-1314.2002.00395.x

Connolly, J. A. D. (1990). Multivariable phase diagrams: An algorithm based on generalized thermodynamics. *American Journal of Science*, *290*, 666–718. https://doi.org/10.2475/ajs.290.6.666

Connolly, J. A. D. (2009). The geodynamic equation of state: What and how. *Geochemistry, Geophysics, Geosystems*, *10*, Q10014.

Cuthbert, S. J., Carswell, D. A., Krogh-Ravna, E. J., & Wain, A. (2000). Eclogites and eclogites in the Western Gneiss region, Norwegian Caledonides. *Lithos*, *52*(1–4), 165–195. https://doi.org/10.1016/S0024-4937(99)00090-0

Dale, J., Powell, R., White, R. W., & Elmer, F. (2005). A thermodynamic model for clinoamphiboles in Na_2O–CaO–FeO–MgO–Al_2O_3–SiO_2–H_2O–O for petrological calculations. *Journal of Metamorphic Geology*, *23*(8), 771–791. https://doi.org/10.1111/j.1525-1314.2005.00609.x

Diener, J. F. A., & Powell, R. (2010). Influence of ferric iron on the stability of mineral assemblages. *Journal of Metamorphic Geology*, *28*(6), 599–613. https://doi.org/10.1111/(ISSN)1525-1314

Diener, J. F. A., & Powell, R. (2012). Revised activity–composition models for clinopyroxene and amphibole. *Journal of Metamorphic Geology*, *30*(2), 131–142. https://doi.org/10.1111/j.1525-1314.2011.00959.x

Faryad, S. W., Klápová, H., & Nosál, L. (2010). Mechanism of formation of atoll garnet during high-pressure metamorphism. *Mineralogical Magazine*, *74*(1), 111–126. https://doi.org/10.1180/minmag.2010.074.1.111

Florence, F. P., & Spear, F. S. (1991). Effects of diffusional modification of garnet growth zoning on P-T path calculations. *Contributions to Mineralogy and Petrology*, *107*(4), 487–500. https://doi.org/10.1007/BF00310683

Forneris, J. F., & Holloway, J. R. (2003). Phase equilibria in subducting basaltic crust: Implications for H 2 O release from the slab. *Earth and Planetary Science Letters*, *214*(1–2), 187–201. https://doi.org/10.1016/S0012-821X(03)00305-4

Franz, G., & Liebscher, A. (2004). Physical and chemical properties of the epidote minerals–An introduction. *Reviews in Mineralogy and Geochemistry*, *56*(1), 1–81. https://doi.org/10.2138/gsrmg.56.1.1

García-Casco, A., Torres-Roldán, R. L., Millán, G., Monié, P., & Schneider, J. (2002). Oscillatory zoning in eclogitic garnet and amphibole, Northern Serpentinite Melange, Cuba: A record of tectonic instability during subduction? *Journal of Metamorphic Geology*, *20*(6), 581–598. https://doi.org/10.1046/j.1525-1314.2002.00390.x

Gilotti, J. A. (2013). The realm of ultrahigh–pressure metamorphism. *Elements*, *9*(4), 255–260. https://doi.org/10.2113/gselements.9.4.255

Giuntoli, F., Lanari, P., & Engi, M. (2018). Deeply subducted continental fragments–Part 1: Fracturing, dissolution–precipitation, and diffusion processes recorded by garnet textures of the central Sesia Zone (western Italian Alps). *Solid Earth*, *9*(1), 167–189. https://doi.org/10.5194/se-9-167-2018

Green, E. C. R., White, R. W., Diener, J. F. A., Powell, R., Holland, T. J. B., & Palin, R. M. (2016). Activity–composition relations for the calculation of partial melting equilibria in metabasic rocks. *Journal of Metamorphic Geology*, *34*(9), 845–869. https://doi.org/10.1111/jmg.12211

Groppo, C., & Castelli, D. (2010). Prograde P-T evolution of a lawsonite eclogite from the Monviso meta–ophiolite (Western Alps): Dehydration and redox reactions during subduction of oceanic FeTi–oxide gabbro. *Journal of Petrology*, *51*(12), 2489–2514. https://doi.org/10.1093/petrology/egq065

Groppo, C., Rolfo, F., & Indares, A. (2012). Partial melting in the Higher Himalayan Crystallines of Eastern Nepal: The effect of

decompression and implications for the 'Channel Flow'model. *Journal of Petrology*, *53*(5), 1057–1088. https://doi.org/10.1093/petrology/egs009

Groppo, C., Rolfo, F., Liu, Y. C., Deng, L. P., & Wang, A. D. (2015). P-T evolution of elusive UHP eclogites from the Luotian dome (North Dabie Zone, China): How far can the thermodynamic modeling lead us? *Lithos*, *226*, 183–200. https://doi.org/10.1016/j.lithos.2014.11.013

Guevara, V. E., & Caddick, M. J. (2016). Shooting at a moving target: Phase equilibria modelling of high–temperature metamorphism. *Journal of Metamorphic Geology*, *34*(3), 209–235. https://doi.org/10.1111/jmg.12179

Hacker, B. R. (2006). Pressures and temperatures of ultrahigh–pressure metamorphism: Implications for UHP tectonics and H_2O in subducting slabs. *International Geology Review*, *48*(12), 1053–1066. https://doi.org/10.2747/0020-6814.48.12.1053

Hacker, B. R., Abers, G. A., & Peacock, S. M. (2003). Subduction factory 1. Theoretical mineralogy, densities, seismic wave speeds, and H_2O contents. *Journal of Geophysical Research: Solid Earth*, *108*(B1), 2029.

Holland, T. J. B., Baker, J., & Powell, R. (1998). Mixing properties and activity composition relationships of chlorites in the system $MgO–FeO–Al_2O_3–SiO_2–H_2O$. *European Journal of Mineralogy*, *10*, 395–406. https://doi.org/10.1127/ejm/10/3/0395

Holland, T. J. B., & Powell, R. (1998). An internally–consistent thermodynamic dataset for phases of petrological interest. *Journal of Metamorphic Geology*, *16*(3), 309–344.

Indares, A., White, R. W., & Powell, R. (2008). Phase equilibria modelling of kyanite-bearing anatectic paragneisses from the central Grenville Province. *Journal of Metamorphic Geology*, *26*(8), 815–836. https://doi.org/10.1111/j.1525-1314.2008.00788.x

Kerrick, D. M., & Connolly, J. A. D. (2001). Metamorphic devolatilization of subducted oceanic metabasalts: Implications for seismicity, arc magmatism and volatile recycling. *Earth and Planetary Science Letters*, *189*(1–2), 19–29. https://doi.org/10.1016/S0012-821X(01)00347-8

Kohn, M. J. (2004). Oscillatory-and sector-zoned garnets record cyclic (?) rapid thrusting in central Nepal. *Geochemistry, Geophysics, Geosystems*, *5*(12).

Konrad-Schmolke, M., Handy, M. R., Babist, J., & O'Brien, P. J. (2005). Thermodynamic modelling of diffusion-controlled garnet growth. *Contributions to Mineralogy and Petrology*, *149*(2), 181–195. https://doi.org/10.1007/s00410-004-0643-6

Konrad-Schmolke, M., O'Brien, P. J., de Capitani, C. D., & Carswell, D. A. (2008). Garnet growth at high–and ultra–high pressure conditions and the effect of element fractionation on mineral modes and composition. *Lithos*, *103*(3–4), 309–332. https://doi.org/10.1016/j.lithos.2007.10.007

Krogh Ravna, E. J. (2000). The garnet–clinopyroxene Fe^{2+}–Mg geothermometer: An updated calibration. *Journal of Metamorphic Geology*, *18*(2), 211–219. https://doi.org/10.1046/j.1525-1314.2000.00247.x

Krogh Ravna, E. J., & Terry, M. P. (2004). Geothermobarometry of UHP and HP eclogites and schists–an evaluation of equilibria among garnet–clinopyroxene–kyanite–phengite–coesite/quartz. *Journal of Metamorphic Geology*, *22*(6), 579–592. https://doi.org/10.1111/j.1525-1314.2004.00534.x

Lanari, P., & Engi, M. (2017). Local bulk composition effects on metamorphic mineral assemblages. *Reviews in Mineralogy and Geochemistry*, *83*(1), 55–102.

Liou, J. G., Tsujimori, T., Zhang, R. Y., Katayama, I., & Maruyama, S. (2004). Global UHP metamorphism and continental subduction/collision: The Himalayan model. *International Geology Review*, *46*(1), 1–27. https://doi.org/10.2747/0020-6814.46.1.1

Massonne, H. J. (2012). Formation of amphibole and clinozoisite–epidote in eclogite owing to fluid infiltration during exhumation in a subduction channel. *Journal of Petrology*, *53*(10), 1969–1998. https://doi.org/10.1093/petrology/egs040

Mattinson, C. G., Menold, C. A., Zhang, J. X., & Bird, D. K. (2007). High-and ultrahigh-pressure metamorphism in the North Qaidam and South Altyn Terranes, western China. *International Geology Review*, *49*(11), 969–995. https://doi.org/10.2747/0020-6814.49.11.969

Mattinson, C. G., Wooden, J. L., Liou, J. G., Bird, D. K., & Wu, C. L. (2006). Age and duration of eclogite–facies metamorphism, North Qaidam HP/UHP terrane. *Western China. American Journal of Science*, *306*(9), 683–711.

Mattinson, C. G., Wooden, J. L., Zhang, J. X., & Bird, D. K. (2009). Paragneiss zircon geochronology and trace element geochemistry, North Qaidam HP/UHP terrane, western China. *Journal of Asian Earth Sciences*, *35*(3–4), 298–309. https://doi.org/10.1016/j.jseaes.2008.12.007

Meyer, J., Mattinson, C. G., & Zhang, J. X. (2015). Fluid release and possible yo–yo subduction recorded by eclogite, North Qaidam UHP terrane, Western China. *Geological Society of America*, Abstracts with Programs *47*(7), 376.

Morimoto, N. (1988). Nomenclature of pyroxenes. *Mineralogy and Petrology*, *39*(1), 55–76.

O'Brien, P. J. (1997). Garnet zoning and reaction textures in overprinted eclogites, Bohemian Massif, European Variscides: A record of their thermal history during exhumation. *Lithos*, *41*(1–3), 119–133. https://doi.org/10.1016/S0024-4937(97)82008-7

Palin, R. M., Reuber, G. S., White, R. W., Kaus, B. J. P., & Weller, O. M. (2017). Subduction metamorphism in the Himalayan ultrahigh–pressure Tso Morari massif: An integrated geodynamic and petrological modelling approach. *Earth and Planetary Science Letters*, *467*, 108–119. https://doi.org/10.1016/j.epsl.2017.03.029

Palin, R. M., St-Onge, M. R., Waters, D. J., Searle, M. P., & Dyck, B. (2014). Phase equilibria modelling of retrograde amphibole and clinozoisite in mafic eclogite from the Tso Morari massif, northwest India: Constraining the P-T–M (H_2O) conditions of exhumation. *Journal of Metamorphic Geology*, *32*(7), 675–693. https://doi.org/10.1111/jmg.12085

Palin, R. M., Weller, O. M., Waters, D. J., & Dyck, B. (2016). Quantifying geological uncertainty in metamorphic phase equilibria modelling: A Monte Carlo assessment and implications for tectonic interpretations. *Geoscience Frontiers*, *7*(4), 591–607. https://doi.org/10.1016/j.gsf.2015.08.005

Pattison, D. R., & Tinkham, D. K. (2009). Interplay between equilibrium and kinetics in prograde metamorphism of pelites: An example from the Nelson aureole, British Columbia. *Journal of Metamorphic Geology*, *27*(4), 249–279. https://doi.org/10.1111/j.1525-1314.2009.00816.x

Pawley, A. R. (1994). The pressure and temperature stability limits of lawsonite–Implications for H_2O recycling in subduction zones. *Contributions to Mineralogy and Petrology*, *118*(8–9), 99–108. https://doi.org/10.1007/BF00310614

Peacock, S. M. (1993). Large–scale hydration of the lithosphere above subducting slabs. *Chemical Geology*, *108*(1–4), 49–59. https://doi.org/10.1016/0009-2541(93)90317-C

Penniston-Dorland, S. C., Kohn, M. J., & Manning, C. E. (2015). The global range of subduction zone thermal structures from exhumed blueschists and eclogites: Rocks are hotter than models. *Earth and Planetary Science Letters*, *428*, 243–254. https://doi.org/10.1016/j.epsl.2015.07.031

Poli, S., & Schmidt, M. W. (2002). Petrology of subducted slabs. *Annual Review of Earth and Planetary Sciences*, *30*(1), 207–235. https://doi.org/10.1146/annurev.earth.30.091201.140550

Powell, R., & Holland, T. J. B. (1999). Relating formulations of the thermodynamics of mineral solid solutions: Activity modelling of pyroxenes, amphiboles, and micas. *American Mineralogist*, *84*(1–2), 1–14. https://doi.org/10.2138/am-1999-1-201

Powell, R., & Holland, T. J. B. (2008). On thermobarometry. *Journal of Metamorphic Geology*, *26*(2), 155–179. https://doi.org/10.1111/j.1525-1314.2007.00756.x

Rebay, G., Powell, R., & Diener, J. F. A. (2010). Calculated phase equilibria for a MORB composition in a P-T range, 450–650 C and 18–28 kbar: The stability of eclogite. *Journal of Metamorphic Geology*, *28*(6), 635–645. https://doi.org/10.1111/(ISSN)1525-1314

Ren, Y., Chen, D., Hauzenberger, C., Liu, L., Liu, X., & Zhu, X. (2016). Petrology and geochronology of ultrahigh–pressure granitic gneiss from South Dulan, North Qaidam belt, NW China. *International Geology Review*, *58*(2), 171–195. https://doi.org/10.1080/00206814.2015.1058729

Roduit, N. (2008). JMICROVISION version 1.2. 7: Image analysis toolbox for measuring and quantifying components of high–definition images.

Rubatto, D., Regis, D., Hermann, J., Boston, K., Engi, M., Beltrando, M., & McAlpine, S. R. (2011). Yo–yo subduction recorded by accessory minerals in the Italian Western Alps. *Nature Geoscience*, *4*(5), 338–342. https://doi.org/10.1038/ngeo1124

Schmidt, M. W. (1995). Lawsonite: Upper pressure stability and formation of higher density hydrous phases. *American Mineralogist*, *80*(11–12), 1286–1292. https://doi.org/10.2138/am-1995-11-1218

Schmidt, M. W., & Poli, S. (1994). The stability of lawsonite and zoisite at high–pressure: Experiments in CASH to 92 kbar and implications for the presence of hydrous phases in subducted lithosphere. *Earth and Planetary Science Letters*, *124*(1–4), 105–118. https://doi.org/10.1016/0012-821X(94)00080-8

Schmidt, M. W., Vielzeuf, D., & Auzanneau, E. (2004). Melting and dissolution of subducting crust at high pressures: The key role of white mica. *Earth and Planetary Science Letters*, *228*(1–2), 65–84. https://doi.org/10.1016/j.epsl.2004.09.020

de Sigoyer, J., Guillot, S., Lardeaux, J. M., & Mascle, G. (1997). Glaucophane–bearing eclogites in the Tso Morari dome (eastern Ladakh, NW Himalaya). *European Journal of Mineralogy*, *9*, 1073–1083. https://doi.org/10.1127/ejm/9/5/1073

Song, S. G., Niu, Y. L., Su, L., Zhang, C., & Zhang, L. F. (2014). Continental orogenesis from ocean subduction, continent collision/subduction, to orogen collapse, and orogen recycling: The example of the North Qaidam UHPM belt, NW China. *Earth-Science Reviews*, *129*, 59–84. https://doi.org/10.1016/j.earscirev.2013.11.010

Song, S. G., Yang, J. S., Xu, Z. Q., Liou, J. G., Wu, C. L., & Shi, R. D. (2003). Metamorphic evolution of the coesite–bearing ultrahigh–pressure terrane in the North Qaidam, northern Tibet, NW China. *Journal of Metamorphic Geology*, *21*(6), 631–664. https://doi.org/10.1046/j.1525-1314.2003.00469.x

Song, S. G., Zhang, L. F., Niu, Y. L., Su, L., Song, B., & Liu, D. Y. (2006). Evolution from oceanic subduction to continental collision: A case study of the Northern Tibetan Plateau inferred from geochemical and geochronological data. *Journal of Petrology*, *47*(3), 435–455. https://doi.org/10.1093/petrology/egi080

Spear, F. S., & Daniel, C. G. (2001). Diffusion control of garnet growth, Harpswell Neck, Maine, USA. *Journal of Metamorphic Geology*, *19*(2), 179–195.

Štípská, P., & Powell, R. (2005). Constraining the P-T path of a MORB-type eclogite using pseudosections, garnet zoning and garnet-clinopyroxene thermometry: An example from the Bohemian Massif. *Journal of Metamorphic Geology*, *23*(8), 725–743.

St-Onge, M. R., Rayner, N., Palin, R. M., Searle, M. P., & Waters, D. J. (2013). Integrated pressure–temperature–time constraints for the Tso Morari dome (Northwest India): Implications for the burial and exhumation path of UHP units in the western Himalaya. *Journal of Metamorphic Geology*, *31*(5), 469–504. https://doi.org/10.1111/jmg.12030

Stowell, H., Zuluaga, C., Boyle, A., & Bulman, G. (2011). Garnet sector and oscillatory zoning linked with changes in crystal morphology during rapid growth, North Cascades, Washington. *American Mineralogist*, *96*(8–9), 1354–1362. https://doi.org/10.2138/am.2011.3759

Syracuse, E. M., van Keken, P. E., & Abers, G. A. (2010). The global range of subduction zone thermal models. *Physics of the Earth and Planetary Interiors*, *183*(1–2), 73–90. https://doi.org/10.1016/j.pepi.2010.02.004

Tomkins, H. S., Powell, R., & Ellis, D. J. (2007). The pressure dependence of the zirconium-in-rutile thermometer. *Journal of Metamorphic Geology*, *25*(6), 703–713. https://doi.org/10.1111/j.1525-1314.2007.00724.x

Tsujimori, T., Sisson, V. B., Liou, J. G., Harlow, G. E., & Sorensen, S. S. (2006). Very–low–temperature record of the subduction process: A review of worldwide lawsonite eclogites. *Lithos*, *92*(3–4), 609–624. https://doi.org/10.1016/j.lithos.2006.03.054

Viete, D. R., Hacker, B. R., Allen, M. B., Seward, G. G., Tobin, M. J., Kelley, C. S, … Duckworth, A. R. (2018). Metamorphic records of multiple seismic cycles during subduction. *Science Advances*, *4*(3), eaaq0234. https://doi.org/10.1126/sciadv.aaq0234

Wei, C. J., & Clarke, G. L. (2011). Calculated phase equilibria for MORB compositions: A reappraisal of the metamorphic evolution of lawsonite eclogite. *Journal of Metamorphic Geology*, *29*(9), 939–952. https://doi.org/10.1111/j.1525-1314.2011.00948.x

Wei, C. J., Cui, Y., & Tian, Z. L. (2015). Metamorphic evolution of LT-UHP eclogite from the south Dabie orogen, central China: An insight from phase equilibria modeling. *Journal of Asian Earth Sciences*, *111*, 966–980. https://doi.org/10.1016/j.jseaes.2015.08.015

Wei, C. J., Li, Y. J., Yu, Y., & Zhang, J. S. (2010). Phase equilibria and metamorphic evolution of glaucophane-bearing UHP eclogites from the Western Dabieshan Terrane, Central China. *Journal of Metamorphic Geology*, *28*(6), 647–666. https://doi.org/10.1111/(ISSN)1525-1314

Wei, C. J., Qian, J. H., & Tian, Z. L. (2013). Metamorphic evolution of medium-temperature ultra-high pressure (MT–UHP) eclogites

from the South Dabie orogen, Central China: An insight from phase equilibria modelling. *Journal of Metamorphic Geology*, *31* (7), 755–774. https://doi.org/10.1111/jmg.12043

Wei, C. J., & Tian, Z. L. (2014). Modelling of the phase relations in high–pressure and ultrahigh–pressure eclogites. *Island Arc*, *23*(4), 254–262. https://doi.org/10.1111/iar.12087

Wei, C. J., Yang, Y., Su, X. L., Song, S. G., & Zhang, L. F. (2009). Metamorphic evolution of low-T eclogite from the North Qilian orogen, NW China: Evidence from petrology and calculated phase equilibria in the system NCKFMASHO. *Journal of Metamorphic Geology*, *27*(1), 55–70. https://doi.org/10.1111/j.1525-1314.2008.00803.x

Weller, O. M., Wallis, S. R., Aoya, M., & Nagaya, T. (2015). Phase equilibria modelling of blueschist and eclogite from the Sanbagawa metamorphic belt of southwest Japan reveals along–strike consistency in tectonothermal architecture. *Journal of Metamorphic Geology*, *33*(6), 579–596. https://doi.org/10.1111/jmg.12134

Whitney, D. L., & Davis, P. B. (2006). Why is lawsonite eclogite so rare? Metamorphism and preservation of lawsonite eclogite, Sivrihisar, Turkey. *Geology*, *34*(6), 473–476. https://doi.org/10.1130/G22259.1

Whitney, D. L., & Evans, B. W. (2010). Abbreviations for names of rock-forming minerals. *American Mineralogist*, *95*(1), 185–187. https://doi.org/10.2138/am.2010.3371

Wilke, F. D. H., O'Brien, P. J., & Altenberger, U. (2010). Multistage reaction history in different eclogite types from the Pakistan Himalaya and implications for exhumation processes. *Lithos*, *114*(1–2), 70–85. https://doi.org/10.1016/j.lithos.2009.07.015

Wu, C., Yang, J. S., Wooden, J. L., Shi, R. D., Chen, S., Meibom, A., & Mattinson, C. G. (2004). Zircon U-Pb SHRIMP dating of the Yematan batholith in Dulan, north Qaidam, NW China. *Chinese Science Bulletin*, *49*(16), 1736–1740. https://doi.org/10.1007/BF03184308

Yang, J. S., Liu, F., Wu, C., Xu, Z., Shi, R., & Chen, S. (2005). Two ultrahigh–pressure metamorphic events recognized in the Central Orogenic Belt of China: Evidence from the U-Pb dating of coesite–bearing zircons. *International Geology Review*, *47*(4), 327–343. https://doi.org/10.2747/0020-6814.47.4.327

Yu, S. Y., Zhang, J. X., & García del Real, P. (2011). Petrology and P-T path of high–pressure granulite from the Dulan area, North Qaidam mountains, northwestern China. *Journal of Asian Earth Sciences*, *42*(4), 641–660. https://doi.org/10.1016/j.jseaes.2010.11.009

Yu, S. Y., Zhang, J. X., Mattinson, C. G., García del Real, P., Li, Y., & Gong, J. (2014). Paleozoic HP granulite–facies metamorphism and anatexis in the Dulan area of the North Qaidam UHP terrane, western China: Constraints from petrology, zircon U-Pb and amphibole Ar–Ar geochronology. *Lithos*, *198*, 58–76. https://doi.org/10.1016/j.lithos.2014.03.016

Zack, T., Rivers, T., Brumm, R., & Kronz, A. (2004). Cold subduction of oceanic crust: Implications from a lawsonite eclogite from the Dominican Republic. *European Journal of Mineralogy*, *16*(6), 909–916. https://doi.org/10.1127/0935-1221/2004/0016-0909

Zhang, G., Ellis, D. J., Christy, A. G., Zhang, L. F., & Song, S. G. (2010). Zr–in–rutile thermometry in HP/UHP eclogites from Western China. *Contributions to Mineralogy and Petrology*, *160* (3), 427–439. https://doi.org/10.1007/s00410-009-0486-2

Zhang, J. X., Mattinson, C. G., Yu, S. Y., Li, J. P., & Meng, F. C. (2010). U-Pb zircon geochronology of coesite–bearing eclogites from the southern Dulan area of the North Qaidam UHP terrane, northwestern China: Spatially and temporally extensive UHP metamorphism during continental subduction. *Journal of Metamorphic Geology*, *28*(9), 955–978. https://doi.org/10.1111/j.1525-1314.2010.00901.x

Zhang, J. X., Meng, F. C., Li, J. P., & Mattinson, C. G. (2009). Coesite in eclogite from the North Qaidam Mountains and its implications. *Chinese Science Bulletin*, *54*(6), 1105–1110.

Zhang, G., Niu, Y. L., Song, S. G., Zhang, L., Tian, Z. L., Christy, A. G., & Han, L. (2015). Trace element behavior and P-T–t evolution during partial melting of exhumed eclogite in the North Qaidam UHPM belt (NW China): Implications for adakite genesis. *Lithos*, *226*, 65–80. https://doi.org/10.1016/j.lithos.2014.12.009

Zhang, J. X., Yu, S. Y., & Mattinson, C. G. (2017). Early Paleozoic polyphase metamorphism in northern Tibet, China. *Gondwana Research*, *41*, 267–289. https://doi.org/10.1016/j.gr.2015.11.009

Zhang, G., Zhang, L., Song, S. G., & Niu, Y. L. (2009). UHP metamorphic evolution and SHRIMP geochronology of a coesite-bearing meta-ophiolitic gabbro in the North Qaidam, NW China. *Journal of Asian Earth Sciences*, *35*(3–4), 310–322. https://doi.org/10.1016/j.jseaes.2008.11.013

SUPPORTING INFORMATION

Additional supporting information may be found online in the Supporting Information section at the end of the article.

Appendix S1. MAN background intensity correction.

Figure S1. Composition profiles of minerals in eclogite D197.

Figure S2. Garnet textural setting, and compositional zoning from eclogite D161B.

Figure S3. Eclogite D197 compositional isopleths for the calculated phase equilibrium diagram.

Figure S4. Eclogite D205 compositional isopleths for the calculated phase equilibrium diagram.

Figure S5. Eclogite D167 compositional isopleths for the calculated phase equilibrium diagram.

Figure S6. Eclogite D161B compositional isopleths for the calculated phase equilibrium diagram.

Figure S7. Eclogite D167 phase equilibrium diagram and peak conditions from Zr in rutile thermometer.

Table S1. Representative microprobe analysis of amphibole and zoisite from studied eclogites from the Dulan area, China.

Table S2. Prograde *P–T* path information from eclogite D161B.

Table S3. Microprobe analyses of minerals used for conventional thermobarometry.

Table S4. Individual trace element concentrations and calculated temperatures of rutile from eclogites from the Dulan area, China.

Table S5. Microprobe analyses from minerals used for conventional thermobarometry sensitivity test of eclogite D205.

Table S6. *P–T* results of the conventional thermobarometry sensitivity test from eclogite D205.

How to cite this article: Hernández-Uribe D, Mattinson CG, Zhang J. Phase equilibrium modelling and implications for *P–T* determinations of medium-temperature UHP eclogites, North Qaidam terrane, China. *J Metamorph Geol*. 2018;36:1237–1261. https://doi.org/10.1111/jmg.12444